

Stability-Aware Training of Machine Learning Force Fields with Differentiable Boltzmann Estimators

Sanjeev Raja

sanjeevr@berkeley.edu

Department of Computer Science, UC Berkeley

Ishan Amin

ishanthewizard@berkeley.edu

Department of Computer Science, Department of Physics, UC Berkeley

Fabian Pedregosa

pedregosa@google.com

Google Deepmind

Aditi Krishnapriyan

aditik1@berkeley.edu

Department of Computer Science, Department of Chemical Engineering, UC Berkeley

Abstract

Machine learning force fields (MLFFs) are an attractive alternative to *ab-initio* methods for molecular dynamics (MD) simulations. However, they can produce unstable simulations, limiting their ability to model phenomena occurring over longer timescales and compromising the quality of estimated observables. To address these challenges, we present Stability-Aware Boltzmann Estimator (StABIE) Training, a multi-modal training procedure which leverages joint supervision from reference quantum-mechanical calculations and system observables. StABIE Training iteratively runs many MD simulations in parallel to seek out unstable regions, and corrects the instabilities via supervision with a reference observable. We achieve efficient end-to-end automatic differentiation through MD simulations using our Boltzmann Estimator, a generalization of implicit differentiation techniques to a broader class of stochastic algorithms. Unlike existing techniques based on active learning, our approach requires no additional *ab-initio* energy and forces calculations to correct instabilities. We demonstrate our methodology across organic molecules, tetrapeptides, and condensed phase systems, using three modern MLFF architectures. StABIE-trained models achieve significant improvements in simulation stability, data efficiency, and agreement with reference observables. By incorporating observables into the training process alongside first-principles calculations, StABIE Training can be viewed as a general semi-empirical framework applicable across MLFF architectures and systems. This makes it a powerful tool for training stable and accurate MLFFs, particularly in the absence of large reference datasets.

1 Introduction

Molecular dynamics (MD) simulation is a staple method of computational science, enabling high-resolution spatiotemporal modeling of atomistic systems throughout biology, chemistry, and materials science Frenkel & Smit (2001). While the atomic forces needed for MD simulation can be obtained on-the-fly via *ab-initio* quantum-mechanical (QM) calculations Car & Parrinello (1985), this is prohibitively expensive for realistic length and time scales Friesner (2005). Machine learning force fields (MLFFs) have recently emerged as a promising option to serve as surrogate models for QM calculations, demonstrating the ability to capture complex many-body interactions, and in some cases transfer flexibly across chemical space Schütt et al. (2018); Hu et al. (2021); Liu et al. (2022); Gasteiger et al. (2021; 2020); Batzner et al. (2022); Musaelian et al. (2022); Batatia et al. (2022); Schütt et al. (2021). Graph neural network (GNN)-based MLFFs trained on large *ab-initio* datasets are increasingly being used to model challenging and important chemical systems with favorable results Merchant et al. (2023); Kozinsky et al. (2023); Chen & Ong (2022); Schaarschmidt et al. (2022); Takamoto et al. (2022); Majewski et al. (2023); Charron et al. (2023); Batatia et al. (2023); Kovács et al. (2023); Shoghi et al. (2023); Gasteiger et al. (2022); Deng et al. (2023).

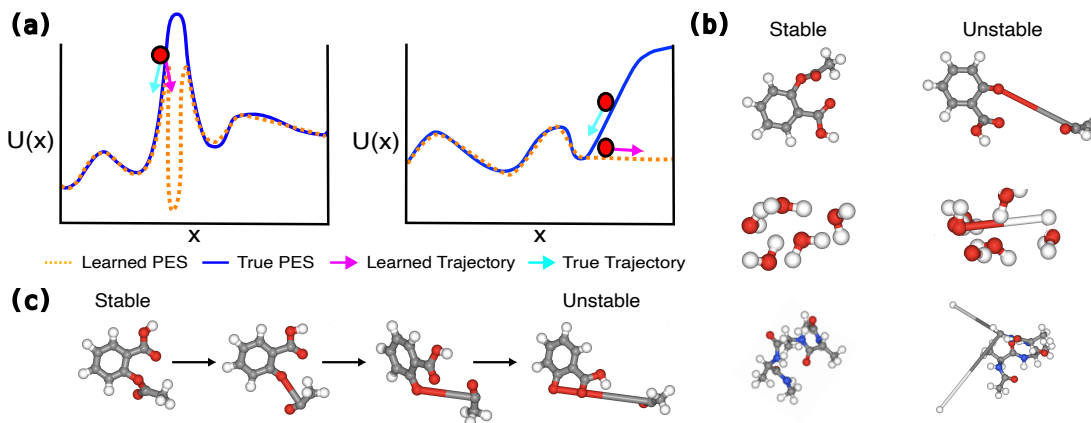


Figure 1: Machine learning force field (MLFF) failure modes. (a) Illustrative examples of true and learned potential energy surfaces (PES) and resulting dynamics for unstable MLFFs. MLFFs can be accurate in approximating much of the PES, but contain regions where energy and forces estimates deviate significantly from the true PES, leading to sampling of highly unphysical regimes. As a result, observables computed from MD simulation may be biased by the oversampling of unphysical states, or have high statistical error in the extreme case of unrecoverable simulation collapse. (b) Examples of stable versus unstable configurations sampled by MLFFs during molecular dynamics simulation of systems considered in this work. (c) Selected states from an unstable MD trajectory of aspirin.

MD simulations aim to accurately estimate system observables like the radial distribution function, virial stress tensor, and diffusivity coefficient. This often requires long simulation to fully explore the underlying PES. Unfortunately, MLFFs are known to produce unstable simulations, meaning that they can irreversibly enter unphysical regions of phase space (e.g., a bond breaking event in a non-reactive system at low temperature) Fu et al. (2022); Stocker et al. (2022); Vita & Schwalbe-Koda (2023); Bihani et al. (2023); Morrow et al. (2023); Wang et al. (2023b). Sampling of such regions can lead to inaccuracies in computed observables as the MLFF gradually drifts from the distribution of its training data. In extreme cases, instabilities can lead to unrecoverable simulation collapse, in which case computed observables may have high statistical error due to insufficient sampling. In either case, instability can limit the ability of MLFF-based MD simulations to investigate long-timescale phenomena like ion diffusion and protein folding, as well as rare events that may require extensive sampling to encounter. Figure 1 illustrates typical MLFF instability behaviors and provides examples of unstable structures sampled during MD simulation.

Simulation instability has been shown to have an unreliable correlation with the energy and force error metrics typically used to train and evaluate MLFFs Fu et al. (2022); Stocker et al. (2022); Bihani et al. (2023). Recent works have introduced alternative simulation-based objectives, such as localized Wang et al. (2023b) or reweighted Ge et al. (2024) energy and force errors, to achieve better downstream stability. However, these approaches do not allow the MLFF to visit new configurations, limiting the distribution over which it is trained and thus the potential improvement. Alternatively, expanding the phase space coverage of the dataset can be an effective way to combat MLFF instability Fu et al. (2022); Stocker et al. (2022); Vita & Schwalbe-Koda (2023); Bihani et al. (2023); Morrow et al. (2023); Wang et al. (2023b). This is typically accomplished via active learning Smith et al. (2018); Vandermause et al. (2020); Schran et al. (2020); Lin et al. (2021); Kulichenko et al. (2023) approaches, where new atomistic configurations are selected, *ab-initio* QM calculations are performed, and the MLFF is retrained on the expanded dataset. However, these techniques rely on performing additional *ab-initio* calculations to expand the dataset. With MLFFs being trained on increasingly diverse datasets Shoghi et al. (2023); Batatia et al. (2023); Kovács et al. (2023) and used to simulate larger atomistic systems, the expense of these calculations may hamper the practicality of active learning workflows. This suggests the need for new training strategies or additional sources of information beyond energies and forces to train stable MLFFs.

In this work, we bridge this gap by using both system observables and *ab-initio* QM data to improve MLFF stability. We introduce **Stability-Aware Boltzmann Estimator (StABIE) Training**, which uses efficient, parallelized MD simulations to rapidly explore regions of molecular phase space where the MLFF becomes unstable, followed by a targeted refinement of these regions using reference system observables. The key to efficient and numerically stable

training lies in the Boltzmann Estimator, which enables end-to-end gradient-based learning without backpropagating directly through MD simulations. We also introduce a localized version of the Boltzmann Estimator, which enables targeted refinement of local instabilities. This is particularly important for stabilizing simulations of large, condensed-phase systems. StABIE Training is a self-contained, efficient process that leverages learning signals from both reference observables and existing QM data, with no reliance on performing additional QM reference calculations.

We demonstrate StABIE Training on three systems and MLFF architectures: 1) simulation of aspirin with SchNet Schütt et al. (2018), 2) simulation of the Ac-Ala3-NHMe tetrapeptide with NequIP Batzner et al. (2022), and 3) simulation of an all-atom water system with GemNet-T Gasteiger et al. (2021). Relative to MLFFs trained solely on energies and forces, our StABIE-trained models produce significantly more stable MD simulations, recover observables more accurately, exhibit better generalization to unseen simulation temperatures, and outperform models trained on 50 times larger, labeled datasets. Our results suggest that utilizing both quantum-mechanical and observable-based modalities is required to fully exploit the available learning signal in reference datasets and train stable and accurate MLFFs. To our knowledge, StABIE Training is the first method that combines these data modalities to improve the stability of neural network potentials in MD simulations.

2 Preliminaries

Molecular Dynamics. Molecular dynamics simulation is used to evolve the positions and momenta of an atomistic system. Given a system of N atoms, its state at time t is defined by $\Gamma(t) = \{r(t), p(t)\}$, where $r(t), p(t) \in \mathbb{R}^{N \times 3}$ are the position and momenta of the atoms. We assume the system has a scalar-valued Hamiltonian function $\mathcal{H} : \mathbb{R}^{N \times 3} \times \mathbb{R}^{N \times 3} \rightarrow \mathbb{R}$ of the form $\mathcal{H}(\Gamma) = \sum_{i=1}^N \frac{p^{(i)2}}{2m^{(i)}} + U(r)$ where $U : \mathbb{R}^{N \times 3} \rightarrow \mathbb{R}$ is a potential energy function and $m^{(i)}$ and $p^{(i)}$ are the mass and momentum of atom i . By updating in the direction of the per-atom forces $-\frac{\partial U}{\partial r}$ using a numerical integration scheme such as Langevin dynamics Bussi & Parrinello (2007), a sequence of K simulation states $\{\Gamma(t)\}_{t=0}^K$ is produced.

Machine Learning Force Fields. A MLFF is a function approximator which learns a potential energy U_θ and forces $F_\theta = -\nabla_r U_\theta = (F_\theta^{(1)}, \dots, F_\theta^{(n)})$ from QM reference data. MLFFs are trained to minimize the following regression loss, with supervision from a dataset of reference energies and forces $\mathcal{D}_{train} = \{(r_i, U_i, F_i)\}_{i=1}^N$.

$$\mathcal{L}_{QM} = \frac{1}{N} \sum_{i=1}^N \left[\lambda_U |U_i(\Gamma) - U_\theta(\Gamma)|^2 + \lambda_F \sum_{j=1}^n \|F_i^{(j)}(\Gamma) + \nabla_{r^{(j)}} U_\theta(\Gamma)\|_2^2 \right] \quad (1)$$

System Observables. Observables, $g(\Gamma(t))$, characterize the state of a MD simulation at time t , and relate to macroscopic properties or experimental measurements of the system. Examples include the radial and angular distribution functions, velocity autocorrelation function, and diffusivity coefficient. Observables can be computed conveniently as an empirical average over states from a MD simulation. This is justified by the ergodicity hypothesis, under which a time-average over a sufficiently long simulation converges to a distributional average over the Boltzmann distribution. More details on the observables used in this work can be found in Supplementary Section A.4.

Training MLFFs with Observables. Observables have been used extensively in the historical development of potentials Cornell et al. (1995); Marrink et al. (2007); Li et al. (2018), and more recently for MLFFs Thaler & Zavadlav (2021); Wang et al. (2020) in the context of condensed-phase Wang et al. (2023a) and titanium Röcken & Zavadlav (2023) systems, enhanced sampling of rare events Šípka et al. (2023), and protein folding simulation Ingraham et al. (2019); Navarro et al. (2023); Kolloff & Olsson (2023). Training with observables requires an efficient way to compute gradients through MD simulations while avoiding numerical instability and memory limitations. The approach is appealing due to the lack of reliance on expensive *ab-initio* quantum mechanical calculations, and the possibility of improved empirical consistency in settings where the underlying *ab-initio* method may be unreliable Cheetham & Seshadri (2024). However, past works do not consider MLFFs with stability problems, and dispense entirely with using QM data, thus losing the first-principles guarantees of matching an *ab-initio* PES.

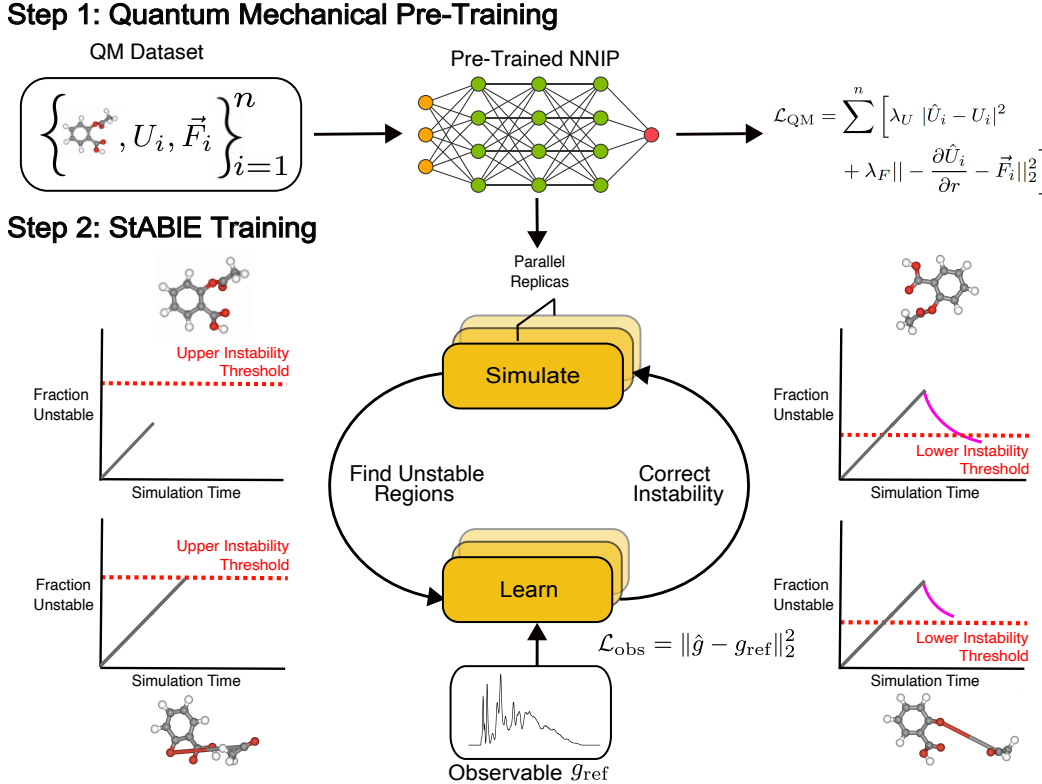


Figure 2: Schematic of Stability-Aware Boltzmann Estimator (StABIE) Training procedure. Our proposed StABIE Training procedure begins with conventional pre-training on a small reference dataset of QM calculations. This dataset remains fixed throughout the procedure, and is never expanded with new calculations. Upon convergence of pre-training, StABIE alternates between two main phases, simulation and learning. In the simulation phase, we perform many molecular dynamics simulations in parallel with the MLFF and find regions of instability. When a sufficient fraction of simulations become unstable, we enter the learning phase, where the MLFF is further trained to match known system observables from *ab-initio* simulation or experiment. Gradients are computed efficiently through the MD simulation via our Boltzmann Estimator. After a sufficient reduction in the portion of unstable trajectories, we re-enter the simulation phase, and repeat the training cycle until a predetermined computational budget is reached.

3 Methods

We present StABIE Training, our proposed procedure to train stable and accurate MLFFs by leveraging both reference quantum mechanical data and system observables. Our approach is enabled by Boltzmann Estimators, which allows gradient-based optimization of MLFFs based on system observables.

3.1 Boltzmann Estimator

Reference system observables can be estimated from high-fidelity MD simulations or experimental measurements. Since observables are linked to the MLFF parameters through a molecular simulation, training with this source of information requires a reliable way to optimize through MD trajectories.

Formally, we define $g(\Gamma)$ to be a vector-valued observable of a state Γ , and g_{ref} to be the reference value of the observable. To train our MLFF to match a reference observable, we minimize the following loss function:

$$\mathcal{L}_{\text{obs}}(\theta) \stackrel{\text{def}}{=} \|\mathbb{E}_{\Gamma \sim P_{\theta}(\Gamma)}[g(\Gamma)] - g_{\text{ref}}\|_2^2, \quad (2)$$

where $P_{\theta}(\Gamma)$ is the equilibrium distribution induced by the MLFF U_{θ} . In this work, we primarily consider systems with a fixed volume, temperature, and number of particles, corresponding to the canonical (NVT) ensemble.

We note, however, that the estimator is readily applicable to other ensembles, including the isothermal/isobaric (NPT) and grand canonical (μVT) ensembles (see Supplementary Sections A.2 and A.10 for details). In the canonical ensemble, microstates obey a Boltzmann distribution, $P_\theta(\Gamma) = \exp\left(-\frac{1}{k_B T} \mathcal{H}_\theta(\Gamma)\right) / C(\theta)$, where $\mathcal{H}_\theta(\Gamma)$ is the Hamiltonian, T is the sampling temperature, k_B is Boltzmann’s constant, and $C(\theta) = \int \exp\left(-\frac{1}{k_B T} \mathcal{H}_\theta(\Gamma')\right) d\Gamma'$ is the normalizing partition function. MD simulation is required at each training iteration to sample from this distribution and estimate the loss.

Optimizing the MLFF requires computing gradients of Equation 2 with respect to θ . The required gradient, $\nabla_\theta \mathcal{L}_{\text{obs}}$, can be decomposed via the chain rule as follows:

$$\nabla_\theta \mathcal{L}_{\text{obs}}^\top = \frac{\partial \mathcal{L}_{\text{obs}}}{\partial \mathbb{E}_{\Gamma \sim P_\theta(\Gamma)}[g(\Gamma)]} \frac{\partial \mathbb{E}_{\Gamma \sim P_\theta(\Gamma)}[g(\Gamma)]}{\partial \theta} = 2(\mathbb{E}_{\Gamma \sim P_\theta(\Gamma)}[g(\Gamma)] - g_{\text{ref}})^\top \frac{\partial \mathbb{E}_{\Gamma \sim P_\theta(\Gamma)}[g(\Gamma)]}{\partial \theta}. \quad (3)$$

The non-trivial quantity to compute is the Jacobian, $\partial \mathbb{E}_{\Gamma \sim P_\theta(\Gamma)}[g(\Gamma)] / \partial \theta$. One way to estimate it is by using a chain rule expansion that corresponds to each step of the unrolled MD simulation Wang et al. (2020). The adjoint method Chen et al. (2019) can be used to limit the memory footprint at the expense of increased computation, but can still lead to numerical instability for long trajectories Wang et al. (2023a); Šípková et al. (2023).

We can avoid direct backpropagation through the simulation by noting that the equilibrium state distribution $P_\theta(\Gamma)$ is independent of the algorithm (i.e., MD integrator) used to sample the distribution. This is analogous to implicit differentiation techniques for differentiable optimization Amos & Kolter (2017); Gould et al. (2016); Ren et al. (2022); Blondel et al. (2022); Négier et al. (2023), in which the solution to an optimization problem is decoupled from the numerical solver used to obtain it. We leverage the known Boltzmann form of $P_\theta(\Gamma)$ to construct an unbiased estimator of the Jacobian.

Definition 1 (*N*-sample Boltzmann estimator). *Given N independent samples $\Gamma_1, \dots, \Gamma_N$ from a Boltzmann distribution $P_\theta(\Gamma)$, we define the N -sample Boltzmann estimator $\mathcal{E}(\Gamma_1, \dots, \Gamma_N)$ of the Jacobian $\partial \mathbb{E}_{\Gamma \sim P_\theta(\Gamma)}[g(\Gamma)] / \partial \theta$ as,*

$$\mathcal{E}(\Gamma_1, \dots, \Gamma_N) = \frac{N}{k_B T (N-1)} \left[\hat{\mathbb{E}}[g(\Gamma)] \hat{\mathbb{E}}[\nabla_\theta U_\theta(\Gamma)]^\top - \hat{\mathbb{E}}[g(\Gamma) \cdot \nabla_\theta U_\theta(\Gamma)^\top] \right], \quad (4)$$

where $\hat{\mathbb{E}}[f(\Gamma)] = \frac{1}{N} \sum_{i=1}^N f(\Gamma_i)$ denotes an empirical mean over the samples.

This estimator provides an unbiased estimate of the Jacobian $\frac{\partial \mathbb{E}_{\Gamma \sim P_\theta(\Gamma)}[g(\Gamma)]}{\partial \theta}$. A proof is provided in Supplementary Section A.1. The estimator is related to the REINFORCE trick Williams (1992) and policy gradient estimators from reinforcement learning Silver et al. (2014) when a Boltzmann state distribution is assumed. The result can also be derived using thermodynamic perturbation theory Zwanzig (1954); Thaler & Zavadlav (2021).

Localized Boltzmann Estimator for Spatial Specificity. In some scenarios, unphysical configurations can occur within localized regions of the simulation domain, such as collisions between two molecules in a large condensed-phase system. Due to spatial averaging, global observables $g(\Gamma)$ may be insensitive to these localized events, limiting the ability to identify unphysical states. To address this, we propose the N -sample Localized Boltzmann Estimator. Here, the global energy $U_\theta(\Gamma)$ and observable $g(\Gamma)$ are replaced with local versions $U_\theta(\gamma)$ and $g(\gamma)$, where γ denotes a local neighborhood of $n < N$ atoms. Formally, define a neighborhood of n atoms $\mathcal{N} = \{x_1, x_2, \dots, x_n \mid x_i \in \mathbb{Z}, 1 \leq x_i \leq N \text{ for all } i=1, 2, \dots, n\}$. The local state γ is defined as $\gamma = \{[r^{(\mathcal{N}_1)}; \dots; r^{(\mathcal{N}_n)}], [p^{(\mathcal{N}_1)}; \dots; p^{(\mathcal{N}_n)}]\}$. The local energy is then defined as $U_\theta(\gamma) = \sum_{i=1}^n U_\theta(\gamma^{(i)})$, where $\gamma^{(i)} = \{r^{(\mathcal{N}_i)}, p^{(\mathcal{N}_i)}\}$ contains the position and momenta of the i^{th} atom in the local neighborhood. The local energy is easily obtained by noting that MLFFs parameterize their global energy prediction U_θ as a sum over individual atomic energies. The localized estimator is thus given as follows:

Definition 2 (N -sample localized Boltzmann estimator). *Given N i.i.d. samples of local states $\gamma_1, \dots, \gamma_N$, where each γ_i is extracted from a global state $\Gamma_i \sim P_\theta(\Gamma)$, we define the N -sample localized estimator of the Jacobian $\frac{\partial \mathbb{E}_{\gamma \sim P_\theta(\gamma)}[g(\gamma)]}{\partial \theta}$ as*

$$\mathcal{E}(\gamma_1, \dots, \gamma_N) \stackrel{\text{def}}{=} \frac{N}{k_B T(N-1)} \left[\hat{\mathbb{E}}[g(\gamma)] \hat{\mathbb{E}}[\nabla_\theta U_\theta(\gamma)]^\top - \hat{\mathbb{E}}[g(\gamma) \cdot \nabla_\theta U_\theta(\gamma)^\top] \right] \quad (5)$$

The localized estimator follows from the original Boltzmann estimator due to the fact that as a subset of the larger Boltzmann-distributed system, any local neighborhood also obeys a Boltzmann-distribution. In practice, we extract multiple local neighborhoods from each global state to increase the sample size and state space coverage (Section A.6). A concrete example of localized instability, along with the use of our localized Boltzmann estimator to correct it, will be presented in the context of an all-atom water system in Results, Section 4.4.

Key Advantages. Unlike active learning approaches, no additional quantum mechanical energy and forces calculations are required to compute our Boltzmann Estimators (all energy terms are model predictions). As a result, learning with the Boltzmann estimator is computationally efficient. Due to the use of independent samples, the estimator also avoids numerical instability and memory demands associated with differentiating through long, continuous trajectories. Further, the most computationally expensive component of the estimator, the gradient of the potential energy $\nabla_\theta U_\theta(\Gamma)$, is independent of the observable $g(\Gamma)$. This means it can be reused, allowing efficient training to match multiple observables simultaneously.

3.2 Stability-Aware Boltzmann Estimator (StABIE) Training

Stability-Aware Boltzmann Estimator (StABIE) Training begins with conventional supervised pre-training of a MLFF on a reference dataset of energy and forces, using the loss defined in Equation 1. The method then proceeds by alternating between two major phases, simulation and learning, as illustrated in Figure 2.

Simulation Phase. The simulation phase aims to explore the molecular phase space and pinpoint regions where the MLFF becomes unstable. We sample R equilibrium states from the training dataset as initial conditions for separate MD trajectories (replicas). Using the pre-trained MLFF U_θ , we run MD simulations on these replicas in parallel for t timesteps. Due to our use of efficient vectorized GPU operations, simulating many replicas in parallel has similar computational cost to simulating a single replica. We apply a predetermined stability criterion (Supplementary Section A.5) to each replica, freezing those marked unstable at their current states. Simulations continue for the remaining replicas, with stability checks every t timesteps. Once a specified fraction of replicas become unstable, we rewind all unstable replicas by t timesteps. This ensures that further simulation for t timesteps will trigger instability, which is then corrected in the next phase. We note that many other strategies exist to explore phase space and find unstable regions, including Diffusion Monte Carlo with fictitious masses Li et al. (2021) or uncertainty-based sampling Kulichenko et al. (2023). StABIE Training can be flexibly used with any of these strategies without impacting the learning stage (described next) of the procedure.

Learning Phase. The learning phase aims to refine the MLFF to correct the previously encountered instabilities. Starting from the near-unstable configurations obtained in the simulation phase, we perform MD simulation for t timesteps, sampling every S^{th} state to obtain uncorrelated samples. Using the sampled states $\Gamma_1, \dots, \Gamma_{N_d}$, where $N_d = \frac{tR}{S}$, we compute the observable loss function (Equation 2). To update the MLFF parameters θ , we compute an unbiased estimator of the loss gradient via the Boltzmann Estimator (Section 3.1) and use it to perform a single step of gradient descent. We then reset all replicas to their original near-unstable states, simulate with the updated MLFF, recompute the loss and gradient estimator with the newly sampled states, and again update the MLFF weights. This process is repeated until the fraction of unstable replicas drops below a predetermined threshold. When this occurs, the learning phase has concluded, and we begin a new simulation phase starting from the endpoints of the last learning phase. We continue alternating between simulation and learning phases until a predetermined computational budget is reached, at which point StABIE Training has concluded. See Supplementary Section A.3 for a formal algorithmic description of the StABIE Training procedure.

Regularizing StABIE Training with Energy and Forces Reference Data. In practice, the mapping between a sparse set of system observables and a potential energy function is non-unique Noid (2013). Consequently, learning

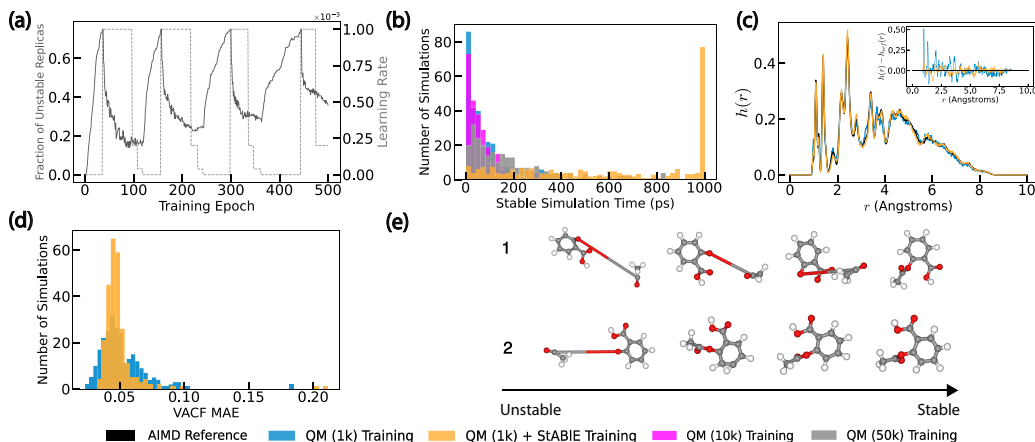


Figure 3: Aspirin simulation with StABIE Training. (a) Alternation of simulation and learning phases during StABIE Training with 128 parallel replicas. The simulation phases correspond to regions where the fraction of unstable replicas increases, while the learning phases correspond to regions where learning occurs and the fraction of unstable replicas decreases. (b) Stable simulation time of 256 parallel aspirin trajectories from SchNet MLFFs. Applying StABIE Training yields significantly more stable simulations than models trained only on energies and forces, surpassing models trained on $50\times$ more QM data. (c) Distribution of interatomic distances ($h(r)$) from MLFF simulations. A StABIE-trained SchNet model closely recovers the true distribution of interatomic distances, while the model trained only on QM reference data produces a noisier $h(r)$ because it cannot stably simulate the system for longer time periods. Inset shows difference between predicted and reference $h(r)$. (d) Distribution of velocity autocorrelation function (VACF) mean absolute error (MAE). StABIE Training yields a reduction in variance across replicas. (e) Aspirin structures sampled over epochs of a single learning phase of StABIE Training. There is a clear progression as unstable configurations become stable.

with observables alone is underconstrained. To combat this, we regularize the observable loss function (Equation 2) with the energy and forces loss function (Equation 1). The final StABIE loss function thus becomes

$$\mathcal{L}_{\text{StABIE}}(\theta) \stackrel{\text{def}}{=} \mathcal{L}_{\text{obs}} + \lambda \mathcal{L}_{\text{QM}}, \quad (6)$$

where \mathcal{L}_{obs} and \mathcal{L}_{QM} were defined in Equations 2 and 1 respectively, and the hyperparameter λ controls the strength of the regularization. Crucially, \mathcal{L}_{QM} is still only computed over the original training dataset $\mathcal{D}_{\text{train}}$, and not over new structures explored during MD simulation. Therefore, the regularization requires no additional quantum mechanical energy and forces calculations.

4 Results

We present the results of StABIE Training on the aspirin molecule with a SchNet MLFF (Section 4.1), the Ac-Ala3-NHMe tetrapeptide with a NequIP MLFF (Section 4.3), and an all-atom water system with a GemNet-T MLFF (Section 4.4).

4.1 Aspirin Molecule

Aspirin (chemical formula $C_9H_8O_4$) is the largest molecule from MD17 Chmiela et al. (2017), a widely used benchmark dataset for atomistic simulations which contains energy and forces calculations computed at the PBE+vdW-TS Tkatchenko & Scheffler (2009) level of theory. Consisting of 21 atoms, aspirin has been shown to be the most challenging molecule in MD17 for state-of-the-art MLFFs to simulate stably Fu et al. (2022). We pre-train a SchNet Schütt et al. (2018) model on the energy and forces matching objective (Equation 1) using a subset of 1,000 aspirin structures from the reference dataset. After convergence, we begin StABIE Training with the global Boltzmann estimator, using 128 parallel replicas at a temperature of 500K. By simulating hundreds of replicas in parallel, we expose the MLFF to a comprehensive range of failure modes much more quickly than

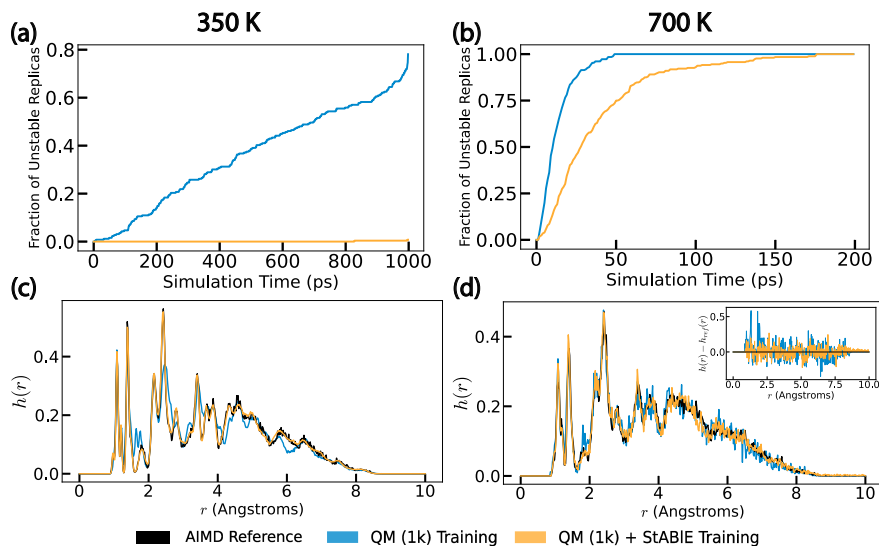


Figure 4: Testing temperature generalization for aspirin. (a, b) Fraction of unstable replicas as a function of simulation time for SchNet MLFFs at 350K and 700K. Applying StABIE Training yields significantly more stable simulations than a baseline SchNet model. (c, d) Distribution of interatomic distances ($h(r)$) from SchNet MLFFs. The StABIE-trained SchNet model more accurately recovers the true $h(r)$ at both 350K and 700K (the inset shows difference between the predicted and reference $h(r)$). The AIMD reference $h(r)$ is computed by Boltzmann-reweighting of independent samples from the 500K training dataset.

possible with a single replica. Following Fu et al. (2022), we use a maximum bond length deviation criterion to detect instability in the simulations (Section A.5). We use the distribution of interatomic distances, $h(r)$, as our training observable, with the $h(r)$ computed over structures in the training dataset serving as the reference (Section A.4). This choice is motivated by the observation that unphysical bond stretches constitute the majority of failure cases in aspirin simulations. The $h(r)$ is sensitive to these abnormalities, and is thus an informative optimization criterion. We perform four complete StABIE cycles of simulation and learning with a SGD optimizer. We evaluate our final models by performing 1 nanosecond constant-temperature MD simulations, starting from 256 initial structures not seen during training. Figure 3a shows the progression of StABIE Training. During the simulation phase, the learning rate is zero and the fraction of unstable replicas steadily increases. When the upper instability threshold is reached, learning commences. The fraction of unstable replicas steadily decreases, confirming that optimization of the interatomic distance distribution produces the desired stability improvement.

A SchNet model trained via our stability-aware approach is significantly more stable during MD simulation than models trained only on the conventional QM energy and forces objective function (Figure 3b). As a result of our training procedure, the median stable simulation time increases from 42 to 602 picoseconds. Even when StABIE training is employed after training on only on 1,000 reference structures, it is more stable than models trained conventionally on 10,000 and 50,000 reference structures, highlighting the effectiveness of our method in improving stability without reliance on any additional QM reference data. We also observe in Supplementary Section A.12 that simply reducing the simulation timestep by a factor of ten does not eliminate instability in simulations produced by conventionally trained models, and reducing instability further may require impractically small timesteps. The stability gains from reducing the timestep are smaller than those resulting from StABIE Training, suggesting that our approach could enable taking larger timesteps and accelerate simulations. Simulations from our model closely recover the true distribution of interatomic distances, while the distributions produced by models solely trained on QM data are noisier, due to the limited stable simulation time (Figure 3c). We also test the ability of our StABIE-trained model to recover the velocity autocorrelation function (VACF), a fundamental dynamical observable not seen during training (Figure 3d). We see that the quality of the recovered VACF remains similar after StABIE Training, with lower variance over the simulated replicas (see Supplementary Section A.13 for a sample VACF computed from the simulations). The preservation of

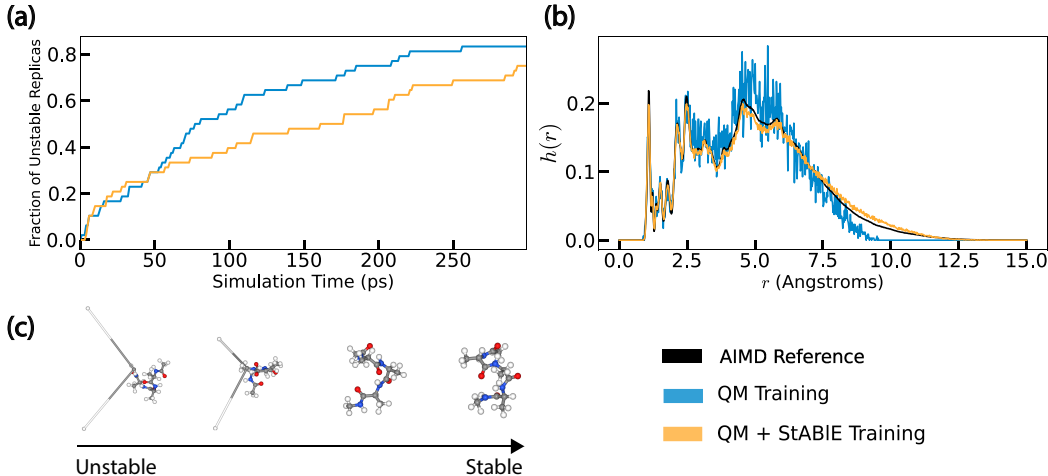


Figure 5: Ac-Ala3-NHMe tetrapeptide simulation with StABIE Training.(a) Fraction of unstable replicas as a function of simulation time for NequIP MLFFs. Applying StABIE Training yields a model which can simulate more MD replicas stably over time than a baseline trained only on energies and forces. (b) Distribution of interatomic distances ($h(r)$) from NequIP MLFF simulations. The StABIE-trained NequIP model much more closely recovers the true $h(r)$, while the $h(r)$ produced by the model trained only on QM reference data is noisy and inaccurate due to insufficient sampling time. (c) Ac-Ala3-NHMe structures sampled over epochs of a single learning phase of StABIE Training. There is a clear progression as very unstable configurations become stable.

a held-out dynamical observable suggests that StABIE Training does not achieve stability improvements by simply restricting the model around a narrow regime corresponding to the reference $h(r)$. If this were the case, characteristic dynamic fluctuations around the reference $h(r)$ would be suppressed, leading to an inaccurate VACF. Figure 3e depicts aspirin structures sampled from simulations during the course of a single learning phase of StABIE Training, demonstrating that unphysical bond stretching in these structures is resolved by the training procedure.

4.2 Temperature generalization

We explore our method’s generalization to different thermodynamic conditions. To do so, we perform 256 parallel MD simulations at 350K and 700K using the SchNet model which was trained with our StABIE Training procedure at 500K. We use the same criterion based on bond length deviation to detect instability as in Section 4.1. We estimate the reference $h(r)$ at 350K and 700K by Boltzmann-reweighting samples from the original 500K training dataset (Section A.9). Aspirin simulations produced by a StABIE-Trained SchNet model are significantly more stable at both temperatures than baseline models trained only on QM reference data (Figure 4a, b). At 350K, the difference is particularly large. After 1 nanosecond of simulation, virtually no replicas are unstable in the StABIE-trained MLFF simulation, while approximately 80% of replicas are unstable in the baseline MLFF simulation. The StABIE-trained model also recovers the true distribution of interatomic distances more closely than the baseline MLFF at both temperatures (Figure 4c, d). At 350K, the baseline MLFF is stable enough produce a smooth $h(r)$, but the structure is inaccurate, indicating incorrect sampling of the phase space. At 700K, the baseline MLFF produces a $h(r)$ which is close to the AIMD-produced distribution, but is noisy due to insufficient stable simulation time. This underscores the necessity for a MLFF to be both stable and accurate in order to be practically useful in MD simulation. StABIE Training improves both of these metrics for this system. As generalization to new thermodynamic conditions is of crucial importance for MLFFs to be useful in practical applications Kovács et al. (2021), we see the temperature-transferability of StABIE Training as an important strength of our method.

4.3 Ac-Ala3-NHMe Tetrapeptide

Ac-Ala3-NHMe (chemical formula $C_{12}H_{22}N_4O_4$) is a tetrapeptide from the MD22 dataset Chmiela et al. (2022), a challenging benchmark consisting of reference energy and forces computed at the PBE+MBD Perdew et al. (1996); Tkatchenko et al. (2012) level of theory for considerably larger molecules than those in the MD17 dataset. Relative to MD17 molecules, Ac-Ala3-NHMe poses unique challenges for atomistic simulations due to its larger

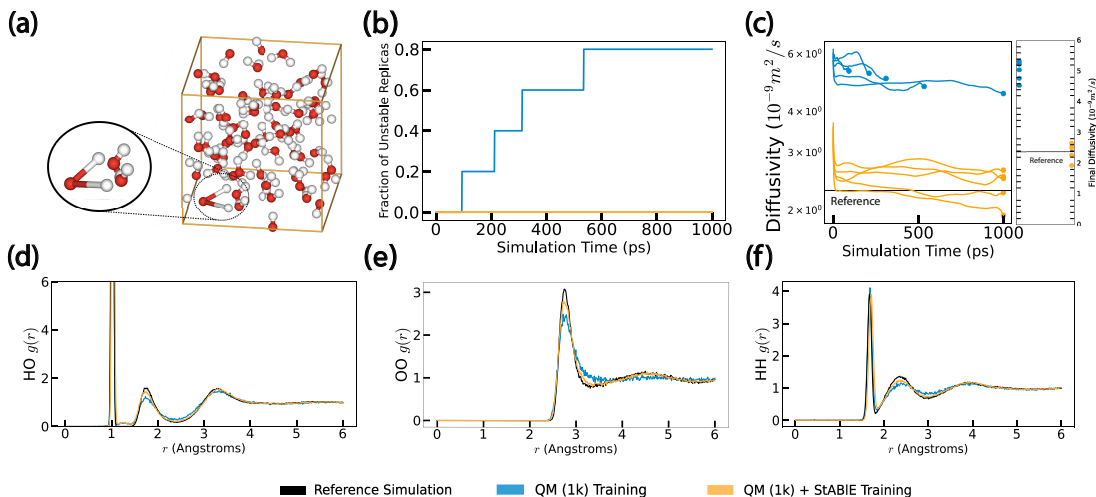


Figure 6: All-Atom Water Simulation with StABIE Training. (a) Example unstable configuration arising in a GemNet-T simulation of water. Instabilities are highly localized and manifest as unphysical bond stretches or intermolecular collisions, motivating the use of our localized Boltzmann estimator (Section 3.1) during training. (b) Fraction of unstable replicas as a function of simulation time for GemNet-T MLFFs. StABIE Training yields a significant stability improvement relative to training on only energy and forces data. (c) Convergence of the diffusivity coefficient over MLFF simulations. The StABIE-trained model gives a considerably more accurate final estimate of the diffusivity coefficient. (d - f) Element-conditioned (OH, OO, HH) radial distribution functions (RDF) produced by MLFF simulations. The StABIE-trained model more accurately captures long-range interactions.

size and flexibility Kabylda et al. (2023). As a result, more expressive MLFFs—sometimes incorporating E(3) equivariance Geiger & Smidt (2022)—are required to accurately model the underlying potential energy surface. In our experiments, we use a NequIP Batzner et al. (2022) model due to its promising accuracy and data efficiency on challenging atomistic simulation tasks Kozinsky et al. (2023); Merchant et al. (2023). We pre-train a NequIP model on the QM energy and forces matching objective using 14,890 (or 25%) of available structures from the training dataset. After convergence, we begin StABIE Training with the global Boltzmann estimator, using 48 parallel replicas at a temperature of 500K. As with aspirin (Sections 4.1 - 4.2), we detect instability using the maximum bond length deviation criterion, and choose the distribution of interatomic distances, $h(r)$, as our training observable. The StABIE-trained NequIP model gives an improvement in stability relative to a baseline model trained only on QM reference data (Figure 5a). Additionally, the StABIE-trained model closely recovers the true $h(r)$, while the baseline MLFF produces a highly noisy $h(r)$. This is because of insufficient sampling, due to a lower stable simulation time (Figure 5b). The baseline MLFF also underestimates the latter portion of the $h(r)$ distribution, indicating poor modelling of long-range interactions. Figure 5c shows selected structures throughout the course of a single learning phase of StABIE Training, demonstrating a progression from very unstable to stable structures.

4.4 Water

As a final evaluation of StABIE Training, we consider liquid-phase water. Water has historically posed unique challenges for atomistic simulations due to the presence of long-range interactions, proton disorder, and nuclear quantum effects Cheng et al. (2019); Raza et al. (2011); Markland & Ceriotti (2018). Additionally, estimating transport properties, such as the diffusivity coefficient, requires long, continuous trajectories to minimize statistical error. We use the dataset produced in Fu et al. (2022), which contains reference all-atom simulations of 64 water molecules using the flexible Extended Simple Point Charge model Wu et al. (2006) at 300K and 1 atm. For this system, we consider a GemNet-T model Gasteiger et al. (2021). GemNet-T displays a failure mode in which unphysical configurations (e.g., bond stretching) first arise in highly localized "pockets" of 1-2 molecules (Figure 6a), which then gradually cascade to the rest of the simulation domain Fu et al. (2022). Such configurations do not noticeably affect global system observables such as the radial distribution function. Therefore, in this setting it is more appropriate to use our localized version of the Boltzmann gradient estimator (Equation 5) in order to guide the optimization process towards specific spatial domains of instability. After pre-training a GemNet-T model using a subset of 1,000 reference struc-

tures, we begin StABIE Training with the localized Boltzmann estimator, simulating 5 parallel replicas at a temperature of 300K. We use a minimum intermolecular distance criterion (Section A.5) to detect instabilities. To estimate gradients for optimization, from each global state we extract all possible local neighborhoods containing a single water molecule (Supplementary Section A.6). The most prevalent failure mode produced by GemNet-T in this system is unphysical bond stretching, which eventually leads to unphysical coordination structures. Motivated by this observation, we use the mean hydrogen-oxygen bond length as our training observable. We perform a single cycle of simulation and learning. We then evaluate the performance of the StABIE-Trained model by performing 5 parallel nanosecond (ns) MD simulations at 300K, starting from held-out initial conditions. We achieve significant improvements in stability and accuracy using our training approach. Our StABIE-trained model can simulate stably for 1 ns for all 5 initial conditions, while the baseline MLFF model trained only on QM reference data can only do so for 1 initial condition, and has a median stability of just 312 ps (Figure 6b). Compared to a reference value of $2.3 \times 10^{-9} \frac{m^2}{s}$, the mean diffusivity produced by StABIE-trained model simulations is $2.4 \times 10^{-9} \frac{m^2}{s}$, while the mean diffusivity produced by baseline model simulations is $1.3 \times 10^{-9} \frac{m^2}{s}$ (Figure 6c). The long-range correlations in the element-conditioned RDFs (Figures 6d-f) are also captured more accurately by the StABIE-trained model. We reiterate that neither the element-conditioned RDFs nor the diffusivity coefficient were explicitly seen during StABIE Training. In Supplementary Section A.10, we demonstrate that StABIE Training leads to similar stability improvements when water simulations are conducted in the isothermal/isobaric (NPT) ensemble, instead of the canonical (NVT) ensemble.

5 Conclusion and Future Work

We have introduced StABIE Training, a strategy for training stable and accurate machine learning force fields. Our training procedure results in MLFFs which are significantly more stable in MD simulation, more accurately reproduce key simulation observables, (including those that were not explicitly trained on), exhibit better generalization to unseen temperatures, and have superior data efficiency relative to MLFFs trained only on QM data.

Key Takeaways. StABIE Training can utilize both quantum-mechanical energies and forces and system observables to supervise MLFF training. We highlight that the reference observables need not be acquired from experimental measurements, and can be computed by averaging over existing QM datasets. This makes our approach applicable in realistic computational discovery scenarios in which experimental characterization is not always available for hypothetical systems. The stability, accuracy, and data efficiency gains brought by StABIE Training require *no additional reference calculations or data*. The procedure is thus self-contained and efficient, requiring minimal additional computational expense beyond a single iteration of conventional MLFF training (see Supplementary Section A.6 for details on training times). This suggests that StABIE Training may scale more gracefully to larger MLFFs and atomistic systems than existing active learning approaches, which require repeated QM reference calculations and retraining. StABIE Training can also be flexibly applied across atomistic systems due to its ability to handle a diverse set of failure modes arising in MD simulation, including both global and local instabilities due to our localized Boltzmann estimator. This flexibility extends to the choice of MLFF: the effectiveness of StABIE Training across the three diverse architectures considered in this work suggests that our approach will remain applicable as MLFF architectures continue to evolve.

Limitations. Unlike traditional QM learning, training MLFFs to match reference observables lacks convergence guarantees in the large data limit. Specifically, the observable-matching objective is under-constrained, as the mapping between a potential energy function and a sparse set of simulation observables is in general non-unique Noid (2013). Although we mitigate this problem by pre-training and regularizing StABIE Training with the conventional energy and forces loss function, we observe that stability improvements resulting from StABIE Training are accompanied by a minor increase in the energy and forces error on a held-out test set, indicating a misalignment between the observable-matching and QM objectives. Adjusting the strength of the QM regularization and the learning rate used for StABIE Training are two primary ways in which to navigate this tradeoff. We note, however, that our observed error increases are typically within the range of DFT error (Supplementary Section A.11). We also note that StABIE Training is currently incompatible with dynamical observables, due to the use of uncorrelated states to compute the Boltzmann Estimator. Overcoming this limitation is non-trivial, as it requires optimization over long paths, which is a significantly higher-dimensional problem with high-variance gradients Bolhuis et al. (2023).

Future Work. In this work, we took observables calculated from high-fidelity simulations as reference values. Many of the observables we considered, such as the radial distribution function, diffusivity coefficient, and equilibrium bond length, are also experimentally measurable. Future work could explore training with experimental

observables from multiple thermodynamic conditions simultaneously to yield more generalizable and robust potentials. Future work could also explore incorporating additional observables into StABIE Training, particularly those which are dynamical. This could restrict the set of learnable functions and address the under-constrained nature of learning with observables. We also note that the reference datasets used to pre-train MLFFs in this work were sampled uniformly from high-fidelity simulations. More sophisticated sampling strategies Deringer et al. (2018); Karabin & Perez (2020); Yoo et al. (2021); Fonseca et al. (2021); Kulichenko et al. (2023); Qi et al. (2024) for diverse dataset generation, as well as during phase space exploration to find unstable regions, could be employed along with StABIE Training to achieve further stability and accuracy gains. Closely related techniques such as active learning are compatible with StABIE Training, and could be used in tandem to further improve MLFF stability and robustness. In this setting, system observables can serve as a cheap source of information with which to augment the more expensive supervision provided by *ab-initio* calculations.

References

- Brandon Amos and J. Zico Kolter. Optnet: Differentiable optimization as a layer in neural networks. In *Proceedings of the International Conference on Machine Learning (ICML)*, pp. 136–145, 2017.
- Ilyes Batatia, David P. Kovacs, Gregor Simm, Christoph Ortner, and Gabor Csanyi. Mace: Higher order equivariant message passing neural networks for fast and accurate force fields. In *Neural Information Processing Systems (NeurIPS)*, 2022.
- Ilyes Batatia, Philipp Benner, Yuan Chiang, Alin M. Elena, Dávid P. Kovács, Janosh Riebesell, Xavier R. Advincula, Mark Asta, William J. Baldwin, Noam Bernstein, Arghya Bhowmik, Samuel M. Blau, Vlad Cărare, James P. Darby, Sandip De, Flaviano Della Pia, Volker L. Deringer, Rokas Elijošius, Zakariya El-Machachi, Edwin Fako, Andrea C. Ferrari, Annalena Genreith-Schriever, Janine George, Rhys E. A. Goodall, Clare P. Grey, Shuang Han, Will Handley, Hendrik H. Heenen, Kersti Hermansson, Christian Holm, Jad Jaafar, Stephan Hofmann, Konstantin S. Jakob, Hyunwook Jung, Venkat Kapil, Aaron D. Kaplan, Nima Karimitari, Namu Kroupa, Jolla Kullgren, Matthew C. Kuner, Domantas Kuryla, Guoda Liepuoniute, Johannes T. Margraf, Ioan-Bogdan Magdău, Angelos Michaelides, J. Harry Moore, Aakash A. Naik, Samuel P. Niblett, Sam Walton Norwood, Niamh O’Neill, Christoph Ortner, Kristin A. Persson, Karsten Reuter, Andrew S. Rosen, Lars L. Schaaf, Christoph Schran, Eric Sivonxay, Tamás K. Stenczel, Viktor Svahn, Christopher Sutton, Cas van der Oord, Eszter Varga-Umbrich, Tejs Vegge, Martin Vondrák, Yangshuai Wang, William C. Witt, Fabian Zills, and Gábor Csányi. A foundation model for atomistic materials chemistry, 2023.
- Simon Batzner, Albert Musaelian, Lixin Sun, Mario Geiger, Jonathan P. Mailoa, Mordechai Kornbluth, Nicola Molinari, Tess E. Smidt, and Boris Kozinsky. E(3)-equivariant graph neural networks for data-efficient and accurate interatomic potentials. *Nature Communications*, 13(1), 5 2022. doi: 10.1038/s41467-022-29939-5.
- Vaibhav Bihani, Utkarsh Pratiush, Sajid Mannan, Tao Du, Zhimin Chen, Santiago Miret, Matthieu Micoulaut, Morten M Smedskjaer, Sayan Ranu, and N M Anoop Krishnan. Egraffbench: Evaluation of equivariant graph neural network force fields for atomistic simulations, 2023.
- Mathieu Blondel, Quentin Berthet, Marco Cuturi, Roy Frostig, Stephan Hoyer, Felipe Llinares-López, Fabian Pedregosa, and Jean-Philippe Vert. Efficient and modular implicit differentiation. In *Neural Information Processing Systems (NeurIPS)*. Google Research, 2022.
- Peter G. Bolhuis, Z. Faidon Brotzakis, and Bettina G. Keller. Optimizing molecular potential models by imposing kinetic constraints with path reweighting. *J. Chem. Phys.*, 159:074102, 2023. doi: 10.1063/5.0151166. URL <https://doi.org/10.1063/5.0151166>.
- Giovanni Bussi and Michele Parrinello. Accurate sampling using langevin dynamics. *Physical Review E—Statistical, Nonlinear, and Soft Matter Physics*, 75(5):056707, 2007.
- R. Car and M. Parrinello. Unified approach for molecular dynamics and density-functional theory. *Phys. Rev. Lett.*, 55:2471, 1985. doi: 10.1103/PhysRevLett.55.2471. Published 25 November 1985.
- Scott P. Carmichael and M. Scott Shell. A new multiscale algorithm and its application to coarse-grained peptide models for self-assembly. *J. Phys. Chem. B*, 116(29):8383–8393, 2012. doi: 10.1021/jp2114994.

-
- Nicholas E. Charron, Felix Musil, Andrea Guljas, Yaoyi Chen, Klara Bonneau, Aldo S. Pasos-Trejo, Jacopo Venturin, Daria Gusew, Iryna Zaporozhets, Andreas Krämer, Clark Templeton, Atharva Kelkar, Aleksander E. P. Durumeric, Simon Olsson, Adrià Pérez, Maciej Majewski, Brooke E. Husic, Ankit Patel, Gianni De Fabritiis, Frank Noé, and Cecilia Clementi. Navigating protein landscapes with a machine-learned transferable coarse-grained model, 2023.
- Anthony K Cheetham and Ram Seshadri. Artificial intelligence driving materials discovery? perspective on the article: Scaling deep learning for materials discovery. *Chemistry of Materials*, 36(8):3490–3495, 2024.
- C. Chen and S.P. Ong. A universal graph deep learning interatomic potential for the periodic table. *Nat Comput Sci*, 2:718–728, 2022. doi: 10.1038/s43588-022-00349-3. URL <https://doi.org/10.1038/s43588-022-00349-3>.
- Ricky T. Q. Chen, Yulia Rubanova, Jesse Bettencourt, and David Duvenaud. Neural ordinary differential equations, 2019.
- Bingqing Cheng, Edgar A. Engel, Jörg Behler, and Michele Ceriotti. Ab initio thermodynamics of liquid and solid water. *Proc. Natl. Acad. Sci. U.S.A.*, 116(4):1110–1115, 1 2019. doi: 10.1073/pnas.1815117116. URL <https://doi.org/10.1073/pnas.1815117116>. Edited by Pablo G. Debenedetti, Princeton University, Princeton, NJ, approved December 3, 2018 (received for review September 4, 2018).
- Stefan Chmiela, Alexandre Tkatchenko, Huziel E. Sauceda, Igor Poltavsky, Kristof T. Schütt, and Klaus-Robert Müller. Machine learning of accurate energy-conserving molecular force fields. *Science Advances*, 3(5), 5 2017. doi: 10.1126/sciadv.1603015.
- Stefan Chmiela, Valentin Vassilev-Galindo, Oliver T. Unke, Adil Kabylda, Huziel E. Sauceda, Alexandre Tkatchenko, and Klaus-Robert Müller. Accurate global machine learning force fields for molecules with hundreds of atoms, 2022.
- Wendy D. Cornell, Piotr Cieplak, Christopher I. Bayly, Ian R. Gould, Kenneth M. Merz, David M. Ferguson, David C. Spellmeyer, Thomas Fox, James W. Caldwell, and Peter A. Kollman. A second generation force field for the simulation of proteins, nucleic acids, and organic molecules. *J. Am. Chem. Soc.*, 117:5179–5197, 1995.
- Bowen Deng, Peichen Zhong, KyuJung Jun, Janosh Riebesell, Kevin Han, Christopher J Bartel, and Gerbrand Ceder. Chgnet as a pretrained universal neural network potential for charge-informed atomistic modelling. *Nature Machine Intelligence*, 5(9):1031–1041, 2023.
- Volker L Deringer, Chris J Pickard, and Gábor Csányi. Data-driven learning of total and local energies in elemental boron. *Physical review letters*, 120(15):156001, 2018.
- FA Faber, L Hutchison, B Huang, J Gilmer, SS Schoenholz, GE Dahl, O Vinyals, S Kearnes, PF Riley, and OA von Lilienfeld. Prediction errors of molecular machine learning models lower than hybrid dft error. *J Chem Theory Comput*, 13(11):5255–5264, 11 2017. doi: 10.1021/acs.jctc.7b00577. Epub 2017 Oct 10.
- Gregory Fonseca, Igor Poltavsky, Valentin Vassilev-Galindo, and Alexandre Tkatchenko. Improving molecular force fields across configurational space by combining supervised and unsupervised machine learning. *The Journal of Chemical Physics*, 154(12), 2021.
- Daan Frenkel and Berend Smit. *Understanding Molecular Simulation: From Algorithms to Applications*. Academic Press, 2 edition, 11 2001.
- Richard A. Friesner. Ab initio quantum chemistry: Methodology and applications. *Proceedings of the National Academy of Sciences*, 102(19):6648–6653, 5 2005. doi: 10.1073/pnas.0408036102.
- Xiang Fu, Zhenghao Wu, Wujie Wang, Tian Xie, Sinan Ketan, Rafael Gomez-Bombarelli, and Tommi Jaakkola. Forces are not enough: Benchmark and critical evaluation for machine learning force fields with molecular simulations, 2022.
- Johannes Gasteiger, Janek Groß, and Stephan Günnemann. Directional message passing for molecular graphs. In *8th International Conference on Learning Representations, ICLR*, 2020.
- Johannes Gasteiger, Florian Becker, and Stephan Günnemann. In *Conference on Neural Information Processing Systems (NeurIPS)*, 2021.

-
- Johannes Gasteiger, Muhammed Shuaibi, Anuroop Sriram, Stephan Günnemann, Zachary Ulissi, C. Lawrence Zitnick, and Abhishek Das. Gemnet-oc: Developing graph neural networks for large and diverse molecular simulation datasets, 2022.
- Fuchun Ge, Ran Wang, Chen Qu, Peikun Zheng, Apurba Nandi, Riccardo Conte, Paul L. Houston, Joel M. Bowman, and Pavlo O. Dral. Tell machine learning potentials what they are needed for: Simulation-oriented training exemplified for glycine. *J. Phys. Chem. Lett.*, 15(16):4451–4460, 2024. doi: 10.1021/acs.jpclett.4c00746. URL <https://doi.org/10.1021/acs.jpclett.4c00746>. Publication Date: April 16, 2024.
- Mario Geiger and Tess Smidt. e3nn: Euclidean neural networks, 2022.
- S. Gould, B. Fernando, A. Cherian, P. Anderson, R. S. Cruz, and E. Guo. On differentiating parameterized argmin and argmax problems with application to bi-level optimization. *arXiv preprint arXiv:1607.05447*, 2016.
- Weihua Hu, Muhammed Shuaibi, Abhishek Das, Siddharth Goyal, Anuroop Sriram, Jure Leskovec, Devi Parikh, and C. Lawrence Zitnick. Forcenet: A graph neural network for large-scale quantum calculations, 2021.
- John Ingraham, Adam Riesselman, Chris Sander, and Debora Marks. Learning protein structure with a differentiable simulator. In *International Conference on Learning Representations, ICLR*, 2019.
- A. Kabylda, V. Vassilev-Galindo, S. Chmiela, I. Poltavsky, and A. Tkatchenko. Efficient interatomic descriptors for accurate machine learning force fields of extended molecules. *Nat Commun*, 14(1):3562, 6 2023. doi: 10.1038/s41467-023-39214-w. Erratum in: *Nat Commun*. 2023 Jul 11;14(1):4116. PMID: 37322039; PMCID: PMC10272221.
- Mariia Karabin and Danny Perez. An entropy-maximization approach to automated training set generation for interatomic potentials. *The Journal of Chemical Physics*, 153(9), 2020.
- Christopher Kolloff and Simon Olsson. Rescuing off-equilibrium simulation data through dynamic experimental data with dynammo. *Mach. Learn.: Sci. Technol.*, 4(4):045050, 2023. doi: 10.1088/2632-2153/ac7b4f. © 2023 The Author(s).
- Dávid Péter Kovács, Cas van der Oord, Jiri Kucera, Alice E. A. Allen, Daniel J. Cole, Christoph Ortner, and Gábor Csányi. Linear atomic cluster expansion force fields for organic molecules: Beyond rmse. *Journal of Chemical Theory and Computation*, 17(12):7696–7711, 2021. doi: 10.1021/acs.jctc.1c00647. URL <https://doi.org/10.1021/acs.jctc.1c00647>. PMID: 34735161.
- Dávid Péter Kovács, J. Harry Moore, Nicholas J. Browning, Ilyes Batatia, Joshua T. Horton, Venkat Kapil, William C. Witt, Ioan-Bogdan Magdău, Daniel J. Cole, and Gábor Csányi. Mace-off23: Transferable machine learning force fields for organic molecules, 2023.
- Boris Kozinsky, Albert Musaelian, Anders Johansson, and Simon Batzner. Scaling the leading accuracy of deep equivariant models to biomolecular simulations of realistic size. In *Proceedings of the International Conference for High Performance Computing, Networking, Storage and Analysis, SC '23*, New York, NY, USA, 2023. Association for Computing Machinery. doi: 10.1145/3581784.3627041. URL <https://doi.org/10.1145/3581784.3627041>.
- Aditi S Krishnapriyan, Alejandro F Queiruga, N Benjamin Erichson, and Michael W Mahoney. Learning continuous models for continuous physics. *Communications Physics*, 6(1):319, 2023.
- M. Kulichenko, K. Barros, N. Lubbers, et al. Uncertainty-driven dynamics for active learning of interatomic potentials. *Nat Comput Sci*, 3:230–239, 2023. doi: 10.1038/s43588-023-00406-5. URL <https://doi.org/10.1038/s43588-023-00406-5>.
- Ask Hjorth Larsen, Jens Jørgen Mortensen, Jakob Blomqvist, Ivano E. Castelli, Rune Christensen, Marcin Dulak, Jesper Friis, Michael N. Groves, Bjørk Hammer, Cory Hargus, et al. The atomic simulation environment — a python library for working with atoms. *Journal of Physics: Condensed Matter*, 2017. doi: 10.1088/1361-648X/aa680e.
- J. Li, C. Qu, and J. M. Bowman. Diffusion monte carlo with fictitious masses finds holes in potential energy surfaces. *Molecular Physics*, 119(17-18), 2021. doi: 10.1080/00268976.2021.1976426. URL <https://doi.org/10.1080/00268976.2021.1976426>.

-
- Xiang-Guo Li, Chongze Hu, Chi Chen, Zhi Deng, Jian Luo, and Shyue Ping Ong. Quantum-accurate spectral neighbor analysis potential models for ni-mo binary alloys and fcc metals. *Phys. Rev. B*, 98:094104, 2018. doi: 10.1103/PhysRevB.98.094104. URL <https://link.aps.org/doi/10.1103/PhysRevB.98.094104>.
- Qidong Lin, Liang Zhang, Yaolong Zhang, and Bin Jiang. Searching configurations in uncertainty space: Active learning of high-dimensional neural network reactive potentials. *J. Chem. Theory Comput.*, 17(5):2691–2701, 2021. doi: 10.1021/acs.jctc.0c01193.
- Yi Liu, Limei Wang, Meng Liu, Yuchao Lin, Xuan Zhang, Bora Oztekin, and Shuiwang Ji. Spherical message passing for 3d molecular graphs. In *International Conference on Learning Representations (ICLR)*, 2022.
- M. Majewski, A. Pérez, P. Thölke, et al. Machine learning coarse-grained potentials of protein thermodynamics. *Nat Commun*, 14:5739, 2023. doi: 10.1038/s41467-023-41343-1. URL <https://doi.org/10.1038/s41467-023-41343-1>.
- TE Markland and M Ceriotti. Nuclear quantum effects enter the mainstream. *Nat Rev Chem*, 2:0109, 2018. doi: 10.1038/s41570-017-0109.
- S. J. Marrink, H. J. Risselada, S. Yefimov, D. P. Tieleman, and A. H. De Vries. The martini force field: coarse grained model for biomolecular simulations. *J. Phys. Chem. B*, 111:7812–7824, 2007. doi: 10.1021/jp071097f.
- A. Merchant, S. Batzner, S.S. Schoenholz, et al. Scaling deep learning for materials discovery. *Nature*, 624:80–85, 2023. doi: 10.1038/s41586-023-06735-9.
- Joe D. Morrow, John L. A. Gardner, and Volker L. Deringer. How to validate machine-learned interatomic potentials. *J. Chem. Phys.*, 158:121501, 2023.
- Albert Musaelian, Simon Batzner, Anders Johansson, Lixin Sun, Cameron J. Owen, Mordechai Kornbluth, and Boris Kozinsky. Learning local equivariant representations for large-scale atomistic dynamics, 2022.
- Carles Navarro, Maciej Majewski, and Gianni De Fabritiis. Top-down machine learning of coarse-grained protein force fields. *J. Chem. Theory Comput.*, 2023.
- Geoffrey Négier, Michael W. Mahoney, and Aditi Krishnapriyan. Learning differentiable solvers for systems with hard constraints. In *The Eleventh International Conference on Learning Representations*, 2023.
- W. G. Noid. Perspective: coarse-grained models for biomolecular systems. *J. Chem. Phys.*, 139:090901, 2013.
- John P. Perdew, Kieron Burke, and Matthias Ernzerhof. Generalized gradient approximation made simple. *Phys. Rev. Lett.*, 77:3865–3868, 10 1996. doi: 10.1103/PhysRevLett.77.3865. URL <https://link.aps.org/doi/10.1103/PhysRevLett.77.3865>.
- Ji Qi, Tsz Wai Ko, Brandon C Wood, Tuan Anh Pham, and Shyue Ping Ong. Robust training of machine learning interatomic potentials with dimensionality reduction and stratified sampling. *npj Computational Materials*, 10(1):43, 2024.
- Z Raza et al. Proton ordering in cubic ice and hexagonal ice; a potential new ice phase-xic. *Phys. Chem. Chem. Phys.*, 13:19788–19795, 2011. doi: 10.1039/c1cp22167a.
- Jie Ren, Xidong Feng, Bo Liu, Xuehai Pan, Yao Fu, Luo Mai, and Yaodong Yang. Torchopt: An efficient library for differentiable optimization, 2022.
- Sebastien Röcken and Julija Zavadlav. Accurate machine learning force fields via experimental and simulation data fusion, 2023.
- Michael Schaarschmidt, Morgane Riviere, Alex M. Ganose, James S. Spencer, Alexander L. Gaunt, James Kirkpatrick, Simon Axelrod, Peter W. Battaglia, and Jonathan Godwin. Learned force fields are ready for ground state catalyst discovery, 2022.

-
- Christoph Schran, Krystof Brezina, and Ondrej Marsalek. Committee neural network potentials control generalization errors and enable active learning. *J. Chem. Phys.*, 153(10):104105, Sep 2020. doi: 10.1063/5.0016004. URL <https://doi.org/10.1063/5.0016004>.
- K. T. Schütt, H. E. Sauceda, P.-J. Kindermans, A. Tkatchenko, and K.-R. Müller. Schnet – a deep learning architecture for molecules and materials. *J. Chem. Phys.*, 148(24):241722, 6 2018. doi: 10.1063/1.5019779. URL <https://doi.org/10.1063/1.5019779>.
- Kristof T. Schütt, Oliver T. Unke, and Michael Gastegger. Equivariant message passing for the prediction of tensorial properties and molecular spectra. In *International Conference on Machine Learning (ICML)*, 2021.
- Nima Shoghi, Adeesh Kolluru, John R. Kitchin, Zachary W. Ulissi, C. Lawrence Zitnick, and Brandon M. Wood. From molecules to materials: Pre-training large generalizable models for atomic property prediction, 2023.
- David Silver, Guy Lever, Nicolas Heess, Thomas Degris, Daan Wierstra, and Martin Riedmiller. Deterministic policy gradient algorithms. In *International conference on machine learning*, pp. 387–395. Pmlr, 2014.
- Justin S. Smith, Ben Nebgen, Nicholas Lubbers, Olexandr Isayev, and Adrian E. Roitberg. Less is more: Sampling chemical space with active learning. *J. Chem. Phys.*, 148:241733, 2018. doi: 10.1063/1.5023802.
- Sina Stocker, Johannes Gasteiger, Florian Becker, Stephan Günnemann, and Johannes T Margraf. How robust are modern graph neural network potentials in long and hot molecular dynamics simulations? *Machine Learning: Science and Technology*, 3(4):045010, 11 2022. doi: 10.1088/2632-2153/ac9955. URL <https://dx.doi.org/10.1088/2632-2153/ac9955>.
- S. Takamoto, C. Shinagawa, D. Motoki, et al. Towards universal neural network potential for material discovery applicable to arbitrary combination of 45 elements. *Nat Commun*, 13:2991, 2022. doi: 10.1038/s41467-022-30687-9. URL <https://doi.org/10.1038/s41467-022-30687-9>.
- Sebastian Thaler and Julija Zavadlav. Learning neural network potentials from experimental data via differentiable trajectory reweighting. *Nature Communications*, 12:6884, 2021. doi: 10.1038/s41467-021-27241-4.
- Alexandre Tkatchenko and Matthias Scheffler. Accurate molecular van der waals interactions from ground-state electron density and free-atom reference data. *Phys. Rev. Lett.*, 102:073005, 2 2009. doi: 10.1103/PhysRevLett.102.073005. URL <https://link.aps.org/doi/10.1103/PhysRevLett.102.073005>.
- Alexandre Tkatchenko, Robert A. DiStasio, Roberto Car, and Matthias Scheffler. Accurate and efficient method for many-body van der waals interactions. *Phys. Rev. Lett.*, 108:236402, 6 2012. doi: 10.1103/PhysRevLett.108.236402. URL <https://link.aps.org/doi/10.1103/PhysRevLett.108.236402>.
- J. Vandermase, S.B. Torrisi, S. Batzner, et al. On-the-fly active learning of interpretable bayesian force fields for atomistic rare events. *npj Comput Mater*, 6:20, 2020. doi: 10.1038/s41524-020-0283-z. URL <https://doi.org/10.1038/s41524-020-0283-z>.
- Joshua A. Vita and Daniel Schwalbe-Koda. Data efficiency and extrapolation trends in neural network interatomic potentials. *Mach. Learn.: Sci. Technol.*, 4:035031, 2023.
- Wujie Wang, Simon Axelrod, and Rafael Gómez-Bombarelli. Differentiable molecular simulations for control and learning, 2020.
- Wujie Wang, Zhenghao Wu, Johannes C. B. Dietschreit, and Rafael Gómez-Bombarelli. Learning pair potentials using differentiable simulations. *The Journal of Chemical Physics*, 158(4):044113, 1 2023a. doi: 10.1063/5.0126475.
- Zun Wang, Hongfei Wu, Lixin Sun, Xinheng He, Zhirong Liu, Bin Shao, Tong Wang, and Tie-Yan Liu. Improving machine learning force fields for molecular dynamics simulations with fine-grained force metrics. *J. Chem. Phys.*, 159:035101, 2023b. doi: 10.1063/5.0147023.
- Ronald J Williams. Simple statistical gradient-following algorithms for connectionist reinforcement learning. *Machine learning*, 1992.

-
- Yujie Wu, Harald L. Tepper, and Gregory A. Voth. Flexible simple point-charge water model with improved liquid-state properties. *The Journal of Chemical Physics*, 124(2):024503, 1 2006. ISSN 0021-9606, 1089-7690. doi: 10.1063/1.2136877.
- Dongsun Yoo, Jisu Jung, Wonseok Jeong, and Seungwu Han. Metadynamics sampling in atomic environment space for collecting training data for machine learning potentials. *npj Computational Materials*, 7(1):131, 2021.
- Robert W. Zwanzig. High-temperature equation of state by a perturbation method. i. nonpolar gases. *J. Chem. Phys.*, 22:1420–1426, 1954.
- Martin Šípka, Johannes C. B. Dietschreit, Lukáš Grajciar, and Rafael Gómez-Bombarelli. Differentiable simulations for enhanced sampling of rare events, 2023.

A Appendix

A.1 Derivation of Boltzmann Estimator

We provide a full derivation of our Boltzmann estimator, which we use to train our MLFF as part of StABIE Training. Consider a vector-valued observable $g(\Gamma)$ of a state Γ , and a reference value of the observable g_{ref} . Training a MLFF U_θ to match g_{ref} requires minimizing the loss function,

$$\mathcal{L}_{\text{obs}}(\theta) \stackrel{\text{def}}{=} \|\mathbb{E}_{\Gamma \sim P_\theta(\Gamma)}[g(\Gamma)] - g_{\text{ref}}\|_2^2,$$

where $P_\theta(\Gamma)$ is the equilibrium distribution induced by the MLFF U_θ . This requires computing the gradient, $\nabla_\theta \mathcal{L}_{\text{obs}}$, which can be decomposed via the chain rule as follows:

$$\begin{aligned} \nabla_\theta \mathcal{L}_{\text{obs}}^\top &= \frac{\partial \mathcal{L}_{\text{obs}}}{\partial \mathbb{E}_{\Gamma \sim P_\theta(\Gamma)}[g(\Gamma)]} \frac{\partial \mathbb{E}_{\Gamma \sim P_\theta(\Gamma)}[g(\Gamma)]}{\partial \theta} \\ &= 2(\mathbb{E}_{\Gamma \sim P_\theta(\Gamma)}[g(\Gamma)] - g_{\text{ref}})^\top \frac{\partial \mathbb{E}_{\Gamma \sim P_\theta(\Gamma)}[g(\Gamma)]}{\partial \theta}. \end{aligned}$$

We derive the N -sample estimator, presented in Equation 6 in the main text, of the Jacobian, $\partial \mathbb{E}_{\Gamma \sim P_\theta(\Gamma)}[g(\Gamma)] / \partial \theta$. The estimator is repeated below for convenience.

$$\mathcal{E}(\Gamma_1, \dots, \Gamma_N) \stackrel{\text{def}}{=} \frac{N}{k_B T (N-1)} \left[\hat{\mathbb{E}}[g(\Gamma)] \hat{\mathbb{E}}[\nabla_\theta U_\theta(\Gamma)]^\top - \hat{\mathbb{E}}[g(\Gamma) \nabla_\theta U_\theta(\Gamma)^\top] \right],$$

where $\hat{\mathbb{E}}$ denotes sample averages. This is an unbiased estimator, that is, $\mathbb{E}_{\Gamma_1, \dots, \Gamma_N \sim P_\theta(\Gamma)}[\mathcal{E}(\Gamma_1, \dots, \Gamma_N)] = \frac{\partial \mathbb{E}_{\Gamma \sim P_\theta(\Gamma)}[g(\Gamma)]}{\partial \theta}$.

Proof. Given $P_\theta(\Gamma) \stackrel{\text{def}}{=} \frac{\exp(-\frac{1}{k_B T} \mathcal{H}_\theta(\Gamma))}{C(\theta)}$, where $\mathcal{H}_\theta(\Gamma) = \sum_{i=1}^N \frac{p_i^2}{2m_i} + U_\theta(r)$, and $C(\theta) \stackrel{\text{def}}{=} \int \exp(-\frac{1}{k_B T} \mathcal{H}_\theta(\Gamma')) d\Gamma'$ is the partition function, we have,

$$\begin{aligned} \frac{\partial \mathbb{E}_{\Gamma \sim P_\theta(\Gamma)}[g(\Gamma)]}{\partial \theta} &= \frac{\partial}{\partial \theta} \int g(\Gamma') P_\theta(\Gamma') d\Gamma' \\ &= \int g(\Gamma') \nabla_\theta P_\theta(\Gamma')^\top d\Gamma' \\ &= \int g(\Gamma') \nabla_\theta \left(\frac{\exp(-\frac{1}{k_B T} \mathcal{H}_\theta(\Gamma'))}{C(\theta)} \right)^\top d\Gamma'. \end{aligned}$$

Expanding via the chain rule for Jacobians, and noting that $\nabla_\theta \mathcal{H}_\theta(\Gamma) = \nabla_\theta U_\theta(r)$ (we will write $U_\theta(\Gamma)$ for convenience) since the kinetic energy is independent of θ , we get,

$$\begin{aligned} \frac{\partial \mathbb{E}_{\Gamma \sim P_\theta(\Gamma)}[g(\Gamma)]}{\partial \theta} &= \int g(\Gamma') \frac{-\frac{1}{k_B T} \exp(-\frac{1}{k_B T} \mathcal{H}_\theta(\Gamma')) \nabla_\theta U_\theta(\Gamma')^\top C(\theta) - \nabla_\theta C(\theta)^\top \exp(-\frac{1}{k_B T} \mathcal{H}_\theta(\Gamma'))}{C(\theta)^2} d\Gamma' \\ &= \int g(\Gamma') \left[-\frac{1}{k_B T} \nabla_\theta U_\theta(\Gamma')^\top P_\theta(\Gamma') - \frac{\nabla_\theta C(\theta)^\top}{C(\theta)} P_\theta(\Gamma') \right] d\Gamma'. \end{aligned}$$

By definition of $C(\theta)$, the quotient $\frac{\nabla_\theta C(\theta)}{C(\theta)}$ can be simplified as,

$$\begin{aligned}
\frac{\nabla_\theta C(\theta)}{C(\theta)} &= \frac{-\int \nabla_\theta U_\theta(\Gamma') \exp\left(-\frac{1}{k_B T} \mathcal{H}_\theta(\Gamma')\right) d\Gamma'}{k_B T \cdot C(\theta)} \\
&= -\frac{1}{k_B T} \int \nabla_\theta U_\theta(\Gamma') P_\theta(\Gamma') d\Gamma' \\
&= -\frac{1}{k_B T} \mathbb{E}_\Gamma[\nabla_\theta U_\theta(\Gamma)].
\end{aligned}$$

Putting it all together, we have,

$$\begin{aligned}
\frac{\partial \mathbb{E}_{\Gamma \sim P_\theta(\Gamma)}[g(\Gamma)]}{\partial \theta} &= -\frac{1}{k_B T} \left(\underbrace{\int g(\Gamma') \nabla_\theta U_\theta(\Gamma')^\top P_\theta(\Gamma') d\Gamma'}_{\mathbb{E}[g(\Gamma) \cdot \nabla_\theta U_\theta(\Gamma)]} - \underbrace{\left(\int g(\Gamma') \cdot P_\theta(\Gamma') \cdot d\Gamma' \right) \mathbb{E}[\nabla_\theta U_\theta(\Gamma)]^\top}_{\mathbb{E}[g(\Gamma)]} \right) \\
&= -\frac{1}{k_B T} (\mathbb{E}[g(\Gamma) \cdot \nabla_\theta U_\theta(\Gamma)^\top] - \mathbb{E}[g(\Gamma)] \mathbb{E}[\nabla_\theta U_\theta(\Gamma)]^\top) \\
&= -\frac{1}{k_B T} \text{Cov}(g(\Gamma), \nabla_\theta U_\theta(\Gamma)).
\end{aligned}$$

In this work, we use the following unbiased estimator for covariance. Given 2 random vectors X, Y , and samples of these vectors $\{(X_1, Y_1), \dots, (X_n, Y_n)\}$, our estimator is given by:

$$\widehat{\text{Cov}}(X, Y) = \frac{1}{N-1} \sum_{i=1}^N X_i Y_i^\top - \frac{1}{N(N-1)} \left(\sum_{j=1}^N X_j \right) \left(\sum_{k=1}^N Y_k^\top \right).$$

We can prove it is unbiased by taking the expectation of the right hand side and applying linearity of expectation:

$$\begin{aligned}
\widehat{\text{Cov}}(X, Y) &= \frac{1}{N-1} \sum_{i=1}^N \mathbb{E}[X_i Y_i^\top] - \frac{1}{N(N-1)} \left(\sum_{i=1}^N \mathbb{E}[X_i Y_i^\top] + \sum_{j \neq k} \mathbb{E}[X_j Y_k^\top] \right) \\
&= \frac{N}{N-1} \mathbb{E}[XY^\top] - \frac{1}{N(N-1)} (N \cdot \mathbb{E}[XY^\top] + N(N-1) \cdot \mathbb{E}[X] \mathbb{E}[Y]^\top) \\
&= \mathbb{E}[XY^\top] - \mathbb{E}[X] \mathbb{E}[Y]^\top = \text{Cov}(X, Y).
\end{aligned}$$

Given the samples $\{\Gamma_1, \dots, \Gamma_N\}$, we can then use the estimator above to get,

$$\begin{aligned}
\widehat{\text{Cov}}(g(\Gamma), \nabla_\theta U_\theta(\Gamma)) &= \frac{1}{N-1} \sum_{i=1}^N g(\Gamma_i) \nabla_\theta U_\theta(\Gamma_i)^\top - \frac{1}{N(N-1)} \left(\sum_{j=1}^N g(\Gamma_j) \right) \left(\sum_{k=1}^N \nabla_\theta U_\theta(\Gamma_k)^\top \right) \\
&= \frac{N}{N-1} \left[\hat{\mathbb{E}}[g(\Gamma) \nabla_\theta U_\theta(\Gamma)^\top] - \hat{\mathbb{E}}[g(\Gamma)] \hat{\mathbb{E}}[\nabla_\theta U_\theta(\Gamma)]^\top \right].
\end{aligned}$$

The final Boltzmann estimator is thus given as,

$$\mathcal{E}(\Gamma_1, \dots, \Gamma_N) \stackrel{\text{def}}{=} \frac{N}{k_B T (N-1)} \left[\hat{\mathbb{E}}[g(\Gamma)] \hat{\mathbb{E}}[\nabla_\theta U_\theta(\Gamma)]^\top - \hat{\mathbb{E}}[g(\Gamma) \nabla_\theta U_\theta(\Gamma)^\top] \right].$$

□

We note that a similar estimator is obtained in Thaler & Zavadlav (2021) by differentiating through a reweighting scheme arising from thermodynamic perturbation theory. We have presented an alternative derivation that does not require reweighting.

A.2 Extension to Other Statistical Ensembles

The Boltzmann Estimator is applicable out-of-the-box to any statistical ensemble where the probability of a microstate can be written as $P_\theta(\Gamma) \propto \exp\left(-\frac{1}{k_B T}[\mathcal{H}_\theta(\Gamma) + \mathcal{X}(\Gamma)]\right)$, where \mathcal{X} contains state-dependent thermodynamic variables. For the isothermal-isobaric (NPT) ensemble, $\mathcal{X}(\Gamma) = pV(\Gamma)$, where p is the simulation pressure and $V(\Gamma)$ is the volume of the microstate. For the grand canonical (μVT) ensemble, $\mathcal{X}(\Gamma) = \mu N(\Gamma)$, where μ is the chemical potential and $N(\Gamma)$ is number of particles in the microstate. For the canonical (NVT) ensemble considered in this work, $\mathcal{X}(\Gamma) = 0$. Since $\mathcal{X}(\Gamma)$ is independent of the MLFF parameters θ in all cases, it can effectively be absorbed into the kinetic energy component of the Hamiltonian, which does not affect the computation of the estimator. Our derivation thus proceeds in the same fashion and yields the same estimator. The Localized Boltzmann Estimator also holds as before.

A.3 StABIE Training Algorithm

We provide an algorithmic description of our StABIE-Training procedure.

Algorithm 1 StABIE Training Procedure

```

1: Initialize:
2: Pre-trained Neural Network Potential  $U_\theta$ 
3: Reference energy and forces dataset  $\mathcal{D}_{\text{train}}$  and observables  $\{g_{\text{ref}}^{(i)}\}_{i=1}^N$ 
4: Simulation length  $t$ , number of parallel replicas  $R$ , minimum unstable threshold  $f_{\text{min}}$ ,
5: maximum unstable threshold  $f_{\text{max}}$ , energy and forces loss weight  $\lambda$ , learning rate  $\alpha$ 
6:
7:  $\bar{\Gamma}_{\text{curr}} \leftarrow \{\Gamma_1(0), \Gamma_2(0), \dots, \Gamma_R(0)\} \sim \mathcal{D}_{\text{train}}$ 
8: Current fraction of unstable replicas  $f_{\text{unst}} \leftarrow 0$ 
9: Total simulated time  $T_{f_i} \leftarrow 0, \forall i = 1, \dots, R$ 
10: Mark all replicas as active for simulation
11: repeat
12:   while  $f_{\text{unst}} < f_{\text{max}}$  do
13:     Simulate active replicas w/  $U_\theta$  for  $t$  steps starting from  $\bar{\Gamma}_{\text{curr}}$ 
14:      $T_{f_i} \leftarrow T_{f_i} + t, \forall i$  corresponding to stable replicas
15:      $\bar{\Gamma}_{\text{curr}} \leftarrow \{\Gamma_1(T_{f_1}), \Gamma_2(T_{f_2}), \dots, \Gamma_R(T_{f_R})\}$ 
16:     Update  $f_{\text{unst}}$  and mark unstable replicas inactive
17:   end while
18:
19:   //  $\bar{\Gamma}_{\text{curr}}$  now contains  $\{\Gamma_1(T_{f_1}), \Gamma_2(T_{f_2}), \dots, \Gamma_R(T_{f_R})\}$ , where  $T_{f_i}$ 's are per-replica total simulation times. At
   // least  $f_{\text{max}}$  fraction of replicas are unstable at this point

20:   while  $f_{\text{unst}} > f_{\text{min}}$  do
21:     Rewind all trajectories by  $t$  timesteps:  $\bar{\Gamma}_{\text{curr}} \leftarrow \{\Gamma_1(T_{f_1} - t), \dots, \Gamma_R(T_{f_R} - t)\}$ 
22:     Simulate all replicas w/  $U_\theta$  for  $t$  steps starting from  $\bar{\Gamma}_{\text{curr}}$ 
23:     Update  $f_{\text{unst}}$ 
24:     Compute observables  $\{\hat{\mathbb{E}}_\Gamma[g^{(i)}(\Gamma)]\}_{i=1}^N$  over all length- $t$  trajectories
25:      $\mathcal{L}_{\text{obs}} \leftarrow \sum_{i=1}^N \|\hat{\mathbb{E}}_\Gamma[g^{(i)}(\Gamma)] - g_{\text{ref}}^{(i)}\|^2$ 
26:      $\mathcal{L}_{\text{QM}} \leftarrow$  energy and forces loss of  $U_\theta$  on dataset  $\mathcal{D}_{\text{train}}$ 
27:      $\theta \leftarrow \theta - \alpha \cdot \nabla_\theta(\mathcal{L}_{\text{obs}} + \lambda \mathcal{L}_{\text{QM}})$  // Compute Boltzmann Estimator
28:   end while
29:   Mark stable replicas active, unstable replicas inactive for next simulation phase
30:   // At most  $f_{\text{min}}$  fraction of replicas are unstable at this point
31: until Convergence or maximum cycles reached

```

}

Simulation Phase

}

Learning Phase

A.4 Observables

We provide definitions and details of the observables considered in this work.

The distribution of interatomic distances serves as a low-dimensional description of 3D structure. For a configuration $r' \in \mathbb{R}^{N \times 3}$, it is defined as,

$$h(r) = \frac{1}{N(N-1)} \sum_{i=1}^N \sum_{j \neq i}^N \delta(r - \|r'_i - r'_j\|),$$

where δ is the Dirac-Delta function. Although the observable need not be differentiable with respect to r for our Boltzmann learning framework, we compute a differentiable version of $h(r)$ via Gaussian smearing as in Wang et al. (2023a) to facilitate comparison with differentiable simulation methods.

The radial distribution function (RDF) captures how density (relative to the bulk) varies as a function of distance from a reference particle, and thus characterizes the structural/thermodynamic properties of the system. The RDF is defined as,

$$RDF(r) = \frac{V}{N^2 4\pi r^2} h(r).$$

where V is the volume of the simulation domain, N is the number of particles, r is the radial distance from a reference particle, and $h(r)$ is a histogram of pairwise distances. As with $h(r)$, we use Gaussian smearing to make the RDF differentiable.

The velocity autocorrelation function (VACF) is an important dynamical observable. Many fundamental properties, such as the diffusion coefficient and vibrational spectra, are functions of this observable. Computing the VACF requires a window of consecutive simulation states to compute. The VACF at a given time lag Δt is given by,

$$VACF(\Delta t) = \frac{1}{S} \sum_{t_0} \sum_i < v_i(t_0), v_i(t_0 + \Delta t) >,$$

where t_0 is an initial time, $v_i(t)$ is the velocity of the i^{th} atom at timestep t , $< \cdot, \cdot >$ is an inner product, and S is the total number of samples considered given the summations over initial times and atoms. In this work, we compute the VACF over a window of 100 consecutive simulation timesteps, and normalize the values by the autocorrelation at $\Delta t = 0$ to restrict the range to $[-1, 1]$.

The diffusivity coefficient is a fundamental transport property with crucial implications on the performance of energy storage systems, among other applications. Related to the time-derivative of the mean squared displacement, the diffusivity coefficient is defined as,

$$D = \lim_{t \rightarrow \infty} \frac{1}{6t} \frac{1}{N} \sum_{i=1}^N |r_i(t) - r_i(0)|^2$$

, where $r_i(t)$ is the coordinate of the i^{th} particle at time t and N is the number of atoms considered. For the water system considered in this work, we measure the diffusivity of all 64 oxygen atoms.

A.5 Stability Criteria

We provide definitions and details on the stability criteria considered in this work.

Adapted from Fu et al. (2022), the maximum bond length deviation metric captures unphysical bond stretching or collapse in small flexible molecules. According to this criterion, a simulation becomes unstable at time T if,

$$\max_{(i,j) \in \mathcal{B}} |(\|r_i(T) - r_j(T)\| - b_{i,j})| > \Delta,$$

where \mathcal{B} is the set of all bonds, i, j are the two endpoint atoms of the bond, and $b_{i,j}$ is the equilibrium bond length computed from the reference simulation. Following Fu et al. (2022), we set $\Delta = 0.5A$ for final stability evaluation. However, we adopt a more conservative value of $\Delta = 0.25A$ during training in order to detect and correct instability earlier. We use this criterion for the MD17 and MD22 datasets.

The minimum intermolecular distance metric is used to detect unphysical coordination structures or collisions between molecules in the water system. According to this criterion, a simulation becomes unstable at time T if,

$$\min_{(i,j) \notin \mathcal{B}} \|r_i(T) - r_j(T)\| < \Delta,$$

where \mathcal{B} is the set of all bonds, and i, j are the endpoint indices of two non-bonded atoms. We set $\Delta = 1.2\text{\AA}$ to detect instability during training.

The minimum intermolecular distance metric is appropriate at train-time to detect instability early before it cascades to the rest of the system. However, it is too sensitive to use for evaluation, as realistic simulation can still be achieved for some time after the occurrence of a highly localized instability. Therefore, following Fu et al. (2022), we adopt an instability metric based on the radial distribution function, defined as,

$$\int_{r=0}^{\infty} \left\| RDF_{\text{ref}}(r) - \langle RDF^t(r) \rangle_{t=T}^{T+\tau} \right\| dr > \Delta,$$

where $\langle \cdot \rangle$ is the averaging operator, τ is a short time window, and Δ is the stability threshold. We use $\tau = 1$ ps and $\Delta = 3.0$ for water. The stability criterion is triggered if any of the three element-conditioned water RDFs (H-H, O-O, or H-O) exceeds the threshold.

A.6 Architecture and Training Details

We provide details on the model architectures and training procedures used in this work. MD simulations and MLFFs are written in the PyTorch framework and are built upon the MDsim Fu et al. (2022) and Atomic Simulation Environment Larsen et al. (2017) packages. All training is performed on a single NVIDIA A100 GPU.

Supplementary Table 1 provides details on the MLFF architectures. r_{max} is the cutoff distance used to construct the radius graph. l_{max} denotes the level of E(3) equivariance used in the network.

	Symmetry Principle	Parameter Count	r_{max} (Å)	l_{max}
SchNet Schütt et al. (2018)	E(3)-invariant	0.12M	5.0	-
NequIP Batzner et al. (2022)	E(3)-equivariant	0.12M	5.0	1
GemNet-T Gasteiger et al. (2021)	SE(3)-equivariant	1.89M	5.0	-

Table 1: MLFF Architecture Details.

For energy and forces pre-training, we follow the protocols in Fu et al. (2022). In order to isolate the effect of observable-based learning, we begin StABIE Training only after pre-training has fully converged (that is, when \mathcal{L}_{QM} has reached a plateau). This means that any improvements in stability or accuracy as a result of StABIE Training can be attributed to the learning signal from the reference observable, as opposed to the regularization from the QM energy and forces data.

We include relevant settings used for StABIE Training in Supplementary Table 2. α is the learning rate, λ is the strength of energy and forces regularization, t is the number of simulation timesteps per epoch, and R is the number of parallel replicas. We note that in practice, we compute the outer products and empirical means in the Boltzmann estimator in batched fashion. Thus, to limit memory usage, we compute $\frac{N}{B}$ separate Boltzmann estimators from minibatches of $B < N$ states and subsequently average them to produce a final estimator.

	MLFF	Stability Criterion, Threshold	Training Observable	Estimator Type	α	λ	t	R	B
Aspirin	SchNet	Bond Len. Dev., 0.25 Å	$h(r)$	Global	0.001	10	2000	128	40
Ac-Ala3-NHMe	NequIP	Bond Len. Dev., 0.25 Å	$h(r)$	Global	0.001	10	2000	128	40
Water	GemNet-T	IMD, 1.2 Å	O-H Bond Length	Local	0.003	0	1000	8	4

Table 2: StABIE Training Settings.

Wall Clock Time of StABIE Training. In Supplementary Table 3, we provide the total wall clock time spent on QM pre-training, as well as the subsequent StABIE Training. All runtimes were measured on an NVIDIA A100 GPU. We note that especially for Ac-Ala3-NHMe and Water, StABIE Training incurs a relatively small marginal computational cost beyond that of QM pre-training.

	QM pre-training	StABIE Training
Aspirin	2	4
Ac-Ala3-NHMe	16	4.7
Water	31	3.5

Table 3: Wall clock time, in hours, of QM pre-training and StABIE Training.

A.7 Simulation Details

We provide MD simulation details in Supplementary Table 4. During training, all systems are simulated with a Nose-Hoover thermostat. During evaluation, either a Nose-Hoover or Langevin thermostat is used based on whichever one yields better stability. Thermostat parameters are chosen to be consistent with prior literature Chmiela et al. (2017; 2022); Fu et al. (2022): for Nose-Hoover simulations, the temperature coupling constant is set to 20 fs, and for Langevin simulations, the friction coefficient is set to 0.1 ps^{-1} .

	Temperature (K)	Timestep (fs)	Periodic Boundary Conditions	Simulation Thermostat
Aspirin	500	0.5	No	Langevin
Ac-Ala3-NHMe	500	0.5	No	Nose-Hoover
Water	300	1	Yes	Nose-Hoover

Table 4: Simulation Settings.

For simulating water in the NPT ensemble at 300K and 1 atm, we employ the Berendsen barostat with temperature and pressure coupling times of 20 fs and 2 ps respectively. We limit the per-timestep change in momentum and volume to 10% and 1% respectively to prevent instabilities resulting from large fluctuations. We found the Berendsen barostat to be more stable than combined Parinello-Rahman and Nose-Hoover dynamics, which would be the more conventional choice for NPT simulations with standard potentials. We speculate that this may be due to qualitative differences in the behavior of ML potentials compared to classical or *ab-initio* potentials, and these differences warrant further investigation in the future.

A.8 Evaluation Details

We provide further details on the protocol used to evaluate the MLFFs considered in this work. Our evaluation protocol is centered around MD simulations. To facilitate direct comparison between StABIE-trained MLFFs and those trained only on energy and forces reference data, for a given molecular system we perform MD simulations starting from the same initial configurations for all models. We choose the number of parallel replicas and total simulation time on a per-system basis so as to saturate GPU memory usage while remaining within a reasonable computational budget. Simulation conditions are the same as described in Section A.7 except for the temperature generalization experiment, in which the temperature of simulation is varied. Supplementary Table 5 summarizes the relevant evaluation parameters for each system.

	Num. Parallel Replicas	Max. Simulation Time (ps)	Stability Criterion, Threshold
Aspirin	256	1000	Bond Length Deviation, 0.5 Å
Ac-Ala3-NHMe	48	300	Bond Length Deviation, 0.5 Å
Water	5	1000	RDF MAE, 3.0

Table 5: StABIE Evaluation Settings.

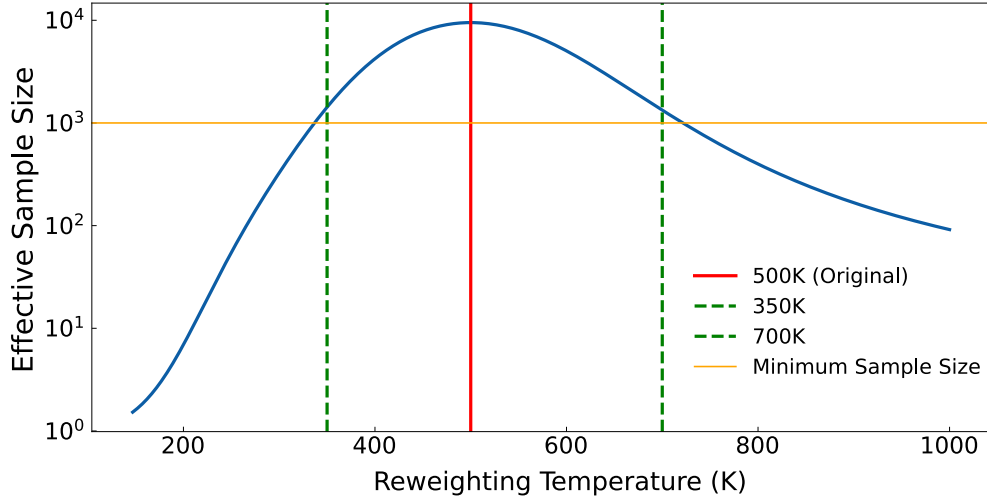


Figure 8: Boltzmann-reweighting of aspirin samples. The effective sample size (N_{eff}) as a function of reweighting temperature for aspirin dataset. N_{eff} is maximized when the reweighting temperature is equal to the original temperature (500K). Using a minimum sample size of 1000, we choose upper and lower temperatures of 700K and 350K at which to perform temperature generalization experiments.

Justification of Chosen Stability Thresholds. Following Fu et al. (2022), we choose stability thresholds such that a realistic, high-fidelity simulation at the chosen temperature would virtually never cross the threshold. This means that if a simulation does cross the threshold, this is indicative of catastrophic failure. Thresholds are set more conservatively during training in order to facilitate early detection of potential collapse. Supplementary Figure 7 shows the distribution of values of the stability criterion over high-fidelity reference simulations for the three systems considered in this work, along with thresholds chosen to denote instability for training and evaluation.

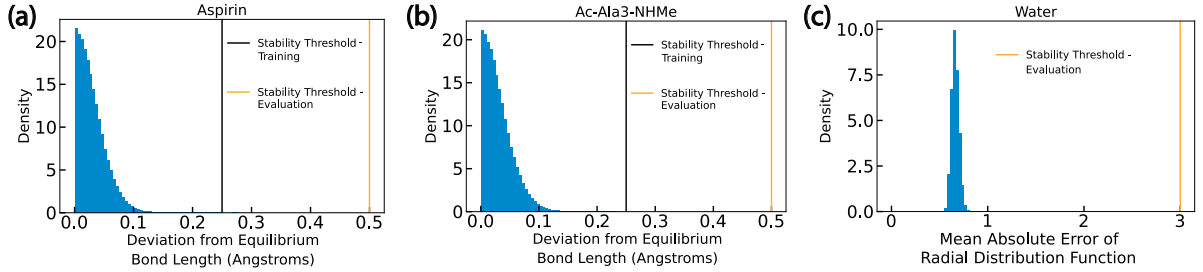


Figure 7: Distribution of stability criterion over reference simulations. Instability thresholds are chosen to be very relaxed, such that crossing of the threshold signifies catastrophic, unrecoverable instability.

A.9 Temperature-Reweighting of Observables

We provide further details on the reweighting process used to estimate the reference distribution of interatomic distances at 350K and 700K. This was used in the temperature generalization experiments described in Section 4.2.

Under the canonical ensemble, microstates follow a Boltzmann distribution $P_\theta(\Gamma) \stackrel{\text{def}}{=} \frac{\exp(-\frac{1}{k_B T} \mathcal{H}_\theta(\Gamma))}{C(\theta)}$. Consider states $\Gamma_1, \dots, \Gamma_N$ sampled at temperature T_1 . Define a reweighting factor for each sample as follows,

$$w_i = \frac{\frac{P_\theta(\Gamma_i; T_1)}{P_\theta(\Gamma_i; T_2)}}{\sum_{i=1}^N \frac{P_\theta(\Gamma_i; T_1)}{P_\theta(\Gamma_i; T_2)}} = \frac{\exp(-\frac{\mathcal{H}_\theta(\Gamma_i)}{k_B} (\frac{1}{T_2} - \frac{1}{T_1}))}{\sum_{i=1}^N \exp(-\frac{\mathcal{H}_\theta(\Gamma_i)}{k_B} (\frac{1}{T_2} - \frac{1}{T_1}))}.$$

We can then compute a reweighted Monte Carlo estimate of the observable at T_2 as follows Thaler & Zavadlav (2021).

$$g_{true, T_2} = \sum_{i=1}^N w_i g(\Gamma_{(i)})$$

The statistical error of the reweighted Monte Carlo estimate is captured by the effective sample size, $N_{eff} \approx e^{-\sum_{i=1}^N w_i \ln(w_i)}$ Carmichael & Shell (2012). A small effective sample size indicates that a few samples with high weights dominate the average; this occurs for large differences between T_1 and T_2 . To select lower and upper temperatures at which to perform the temperature generalization experiment, we set a minimum $N_{eff} = 1000$, leading us to choose 350K and 700K (Figure 8).

A.10 StABIE Training in the Isothermal-Isobaric Ensemble

We repeat StABIE Training on the all-atom water system, and this time simulate in the isothermal-isobaric (NPT) ensemble with a temperature of 300K and a pressure of 1 atm. We use the same training settings outlined in Supplementary Table 2. We find similar results to when we simulate in the canonical (NVT) ensemble: StABIE Training yields clear stability improvements, increasing the median stable simulation time from 51 to 165 picoseconds. The stability and quality of estimated observables is slightly lower than in NVT simulations, including some unphysical collisions in the short-range region of the element-conditioned RDFs. This may be due to the distribution shift induced by the continuously changing box size in NPT simulations, which was not seen during pretraining of the GemNet-T potential.

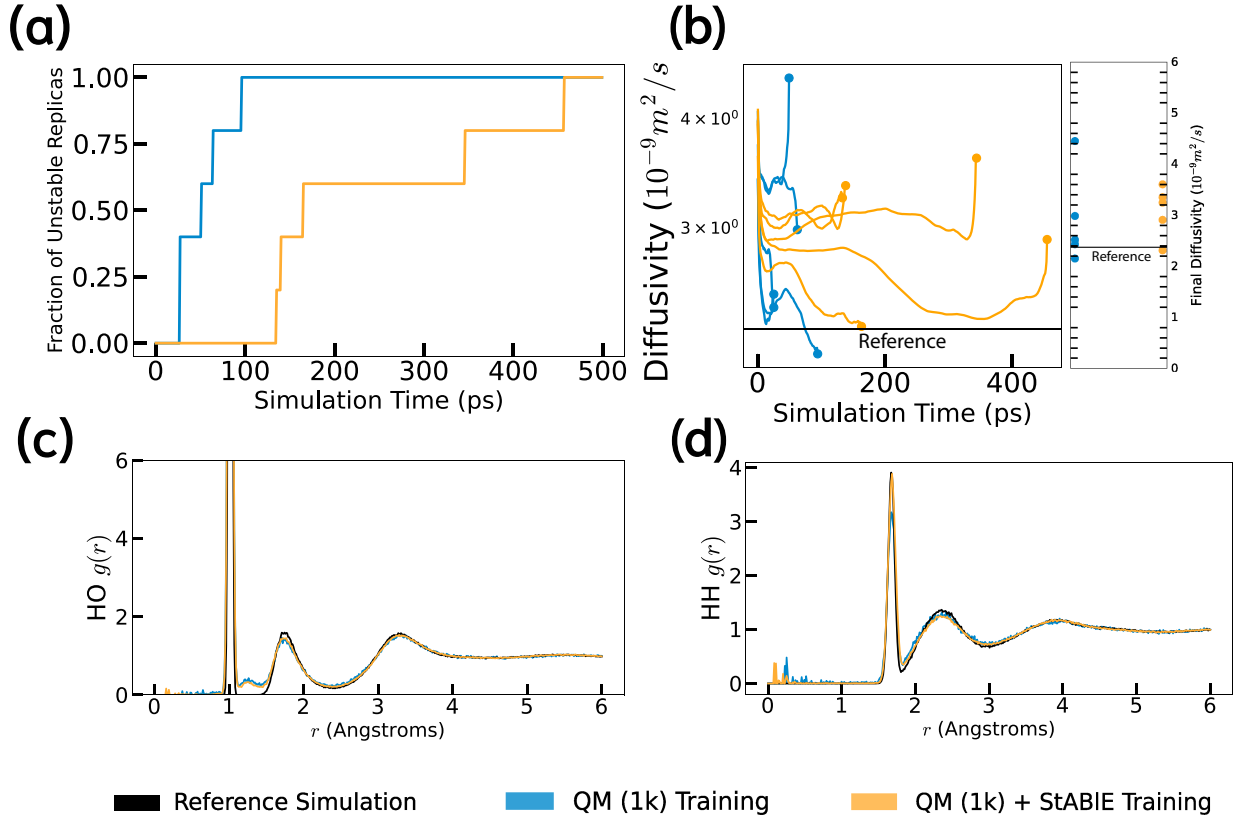


Figure 9: Results of StABIE Training a GemNet-T model for all-atom water simulation in the isothermal-isobaric (NPT) ensemble. StABIE Training yields considerable improvements in stable simulation time, and maintains or slightly improves the accuracy of recovered observables.

A.11 Analysis of Energy and Forces Errors

We study the effect of two hyperparameters of StABIE Training, the learning rate α and the strength of QM regularization λ , on the energy and forces errors of a SchNet MLFF on a held-out test set of aspirin structures. We perform StABIE Training for learning rates ranging from 10^{-5} to 10^{-3} and QM regularization coefficients ranging from 10^0 to 10^2 . We perform evaluation of each trained model via MD simulation of 256 parallel replicas at 500K.

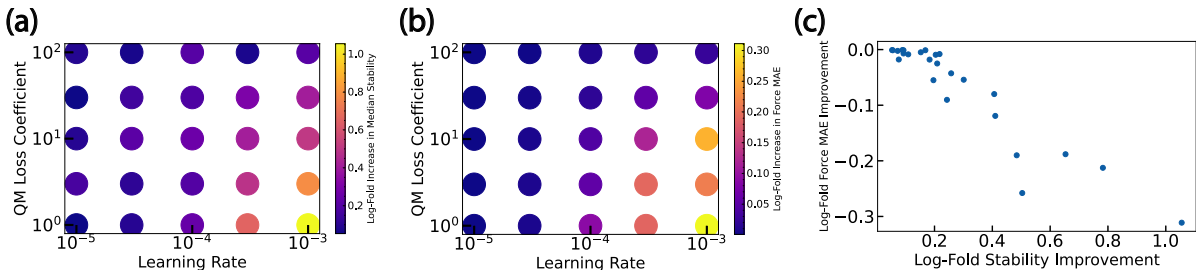


Figure 10: Effect of training hyperparameters on stability and force error improvements. (a) Models trained with higher learning rate and lower QM loss coefficient achieve better stability gains relative to a baseline model trained only on QM reference data. (b) Models trained with higher learning rate and lower QM loss coefficient incur higher increases in force mean absolute error (MAE) on a held-out test dataset relative to the baseline model. (c) A Pareto frontier of Stability vs Force MAE arises. Some choices of learning rate and loss coefficient are Pareto-suboptimal, while choosing others moves along the Pareto frontier.

Training runs with high learning rate and low QM loss coefficient achieve greater improvements in stable simulation time relative to a baseline model trained only on QM reference data (Supplementary Figure 10a). However, these training runs also incur a greater increase in the Mean Absolute Error (MAE) of force prediction on a held out test dataset (Supplementary Figure 10b). Due to training on a single structural observable, the observable-matching component of the StABIE objective is ill-posed: a MLFF which collapses simulations onto a sparse set of states exactly matching the reference observable would globally minimize the observable-matching loss and yield indefinitely stable simulations, while incurring a large QM/force error. As the learning rate of the StABIE Training procedure is increased, the optimization is increasingly pushed towards this degenerate mode. Increasing the weight of the QM objective counteracts this tendency. Consequently, a Pareto frontier arises between stability and force prediction accuracy (Supplementary Figure 10c). Some settings of learning rate and QM loss coefficient are Pareto suboptimal, while choosing among the remaining combinations causes one to move along the frontier. Incorporating additional training observables, particularly those which are dynamical in nature (e.g., velocity autocorrelation functions), could counteract the degeneracy and push the Pareto frontier outwards.

Finally, we note that the observed energy MAE increase on aspirin for our chosen combination of learning rate ($\alpha = 0.001$) and loss coefficient ($\lambda = 10$) is from 0.87 to 1.4 kcalmol^{-1} , while DFT error for energies on MD17 can be as high as 2.3 kcalmol^{-1} Faber et al. (2017). Thus, some of the error in the MLFF predictions could be attributable to inaccuracies in the underlying DFT data.

A.12 Effect of Simulation Timestep on Stability

We perform 100 ps simulations using various timesteps for the aspirin and Ac-Ala3-NHMe tetrapeptide systems, using a SchNet and NequIP potential respectively (Supplementary Figure 11).

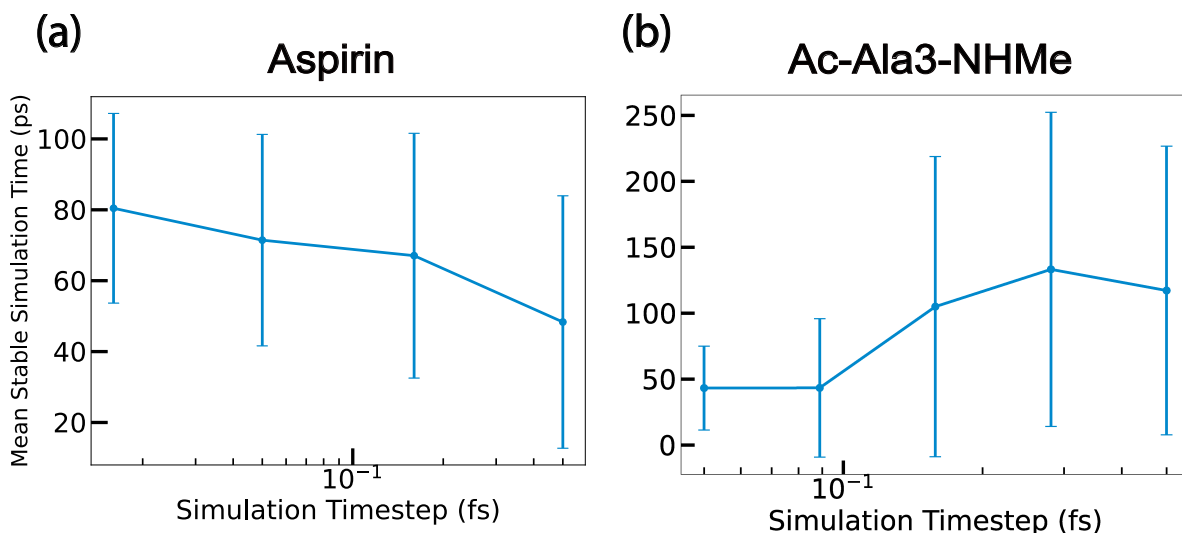


Figure 11: Effect of timestep on simulation stability. Reducing the timestep does not completely eliminate instability, and can sometimes worsen stability.

We observe that instability is not completely eliminated as the timestep is reduced. For the tetrapeptide system, stability consistently decreases as the timestep is reduced. Similar behavior has been observed in neural network based solvers for ordinary differential equations Krishnapriyan et al. (2023). For the aspirin system, stability improves as the timestep is reduced, but does so very slowly (simulations are not completely stable even with a timestep of 0.05 fs, which is 10 times lower than the original timestep).

A.13 Velocity Autocorrelation Function of Aspirin

We show the aspirin velocity autocorrelation function (VACF) corresponding to the trajectory with the median stability improvement between conventional and StABIE Training. A StABIE-trained model produces a similar VACF relative to a conventionally trained model. This suggests that the StABIE procedure does not significantly interfere with dynamic properties of the simulation, despite only training with a structural observable ($h(r)$).

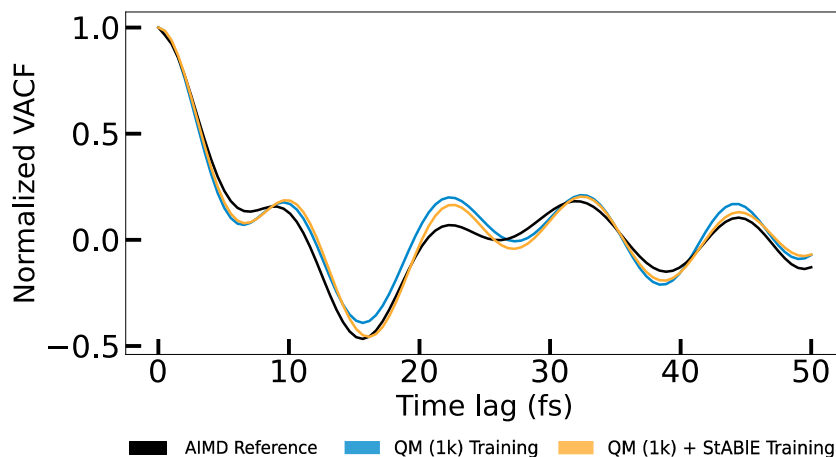


Figure 12: Velocity autocorrelation function of aspirin.